Spatial variations in late Quaternary slip rates along the Doruneh Fault System (Central Iran)

Yassaman Farbod, Esmaeil Shabanian, Olivier Bellier, Mohammad Reza Abbassi, Regis Braucher, Lucilla Benedetti, Didier Bourles, Khaled Hessami

AGU PUBLICATIONS

Tectonics

RESEARCH ARTICLE
10.1002/2015TC003862

Key Points:
- Cosmic ray exposure dating of the Late Quaternary alluvial abandonments surfaces
- Slip rates variation and seismogenic behavior of the Doruneh Fault System

Supporting Information:
- Figures S1–S17

Correspondence to:
E. Shabanian,
shabanian@iasbs.ac.ir

Citation:
Farbod, Y., E. Shabanian, O. Bellier, M. R. Abbassi, R. Braucher, L. Benedetti, D. Bourlès, and K. Hessami (2016), Spatial variations in late Quaternary slip rates along the Doruneh Fault System (Central Iran), *Tectonics*, *35*, 386–406, doi:10.1002/2015TC003862.

Received 20 FEB 2015
Accepted 15 JAN 2016
Accepted article online 21 JAN 2016
Published online 18 FEB 2016

Spatial variations in late Quaternary slip rates along the Doruneh Fault System (Central Iran)

Yassaman Farbod[1], Esmaeil Shabanian[1,2], Olivier Bellier[1], Mohammad Reza Abbassi[3], Régis Braucher[1], Lucilla Benedetti[1], Didier Bourlès[1], and Khaled Hessami[3]

[1]Aix-Marseille Université, CNRS, IRD, CEREGE UM34, Aix-en-Provence, France, [2]Now at Institute for Advanced Studies in Basic Sciences, Zanjan, Iran, [3]International Institute of Earthquake Engineering and Seismology, Tehran, Iran

Abstract The Doruneh Fault System (DFS) is one of the major active strike-slip faults in the Arabia-Eurasia collision zone. Despite its geological activity, no large ($M \geq 6.5$) historical or instrumental earthquakes have been recorded along it. To date, the rate and distribution of slip, as well as the seismic behavior of the DFS, have been unknown. We reconstructed 67 geomorphic offsets recorded by three successive alluvial abandonment surfaces (Q1, Q2, and Q3) displaced along the western (WFZ) and central (CFZ) fault zones. The determined ages of ~12, ~36, and ~120 ka, using in situ-produced ^{10}Be and ^{36}Cl cosmogenic nuclides for theses surfaces, allowed to estimate three sets of individual left-lateral slip rates and consequently to describe the spatiotemporal distribution of slip along the CFZ and WFZ. The slip rates averaged over time intervals of ~36 and ~120 ka reveal variable slip rates along length but similar slip rates at a point with a maximum rate of ~8.2 mm/yr. During the Holocene, however, the fault slip behavior appears more complex, with a maximum rate of ~5.3 mm/yr. The CFZ is divided into two ~4 km apart segments, with symmetrical slip distributions relative to a persistent boundary, which has not been ruptured over the last ~12 ka. The maximum length of seismic fault segments varies from 70 to 100 km, which could produce earthquakes with a magnitude of M_w 7.2–7.4. This emphasizes the necessity of segmentation models for long strike-slip faults that may not necessarily rupture along their whole length during a single earthquake.

1. Introduction

Geological slip rates derived from the relevant ages and amounts of geomorphic/geologic fault offsets are generally averaged over thousands to hundred thousand years [e.g., *Ritz et al.*, 2003; *Siame et al.*, 1997; *Philip et al.*, 2001; *Hessami et al.*, 2006; *Rizza et al.*, 2011; *Shabanian et al.*, 2009a]. They therefore cover a large number of seismic cycles and lead to the better understanding of (1) the role of active faults in the accommodation of regional deformation and (2) the seismic behavior of faults that helps in seismic hazard assessment and the development of physical earthquake models.

This study is focused on the slip behavior and seismic characteristics of the Doruneh Fault System (DFS). The ~400 km long DFS is one of the largest strike-slip faults of the Iranian plateau [e.g., *Wellman*, 1966; *Tchalenko et al.*, 1973] along which few active tectonic studies have been carried out [e.g., *Berberian and Yeats*, 1999; *Fattahi et al.*, 2007; *Farbod et al.*, 2011]. The structural and geomorphic investigations by *Farbod et al.* [2011] led to a preliminary segmentation model according to which (1) the DFS is divided into three fault zones having distinct structural and geomorphic characteristics and (2) independent seismic segments could not exceed the length of ~140 km. However, the distribution and rate of slip on the fault zones, as well as the true extent of the segments, remain poorly known.

In this study, we used the GeoEye© images (Google Earth) to systematically reconstruct left-lateral geomorphic offsets recorded by three generations of alluvial fans (Q1, Q2, and Q3) affected by the DFS all along the fault. In addition, we determined the surface abandonment exposure ages of these three generations of alluvial fans, using in situ-produced ^{10}Be and ^{36}Cl cosmogenic nuclides. These original data were used to evaluate the distribution and variation in space and time of Quaternary left-lateral slip rates along strike of the DFS.

2. Tectonic Setting and General Geology

The Iranian plateau is deformed between the Arabian and Eurasian plates converging at a maximum rate of 26 ± 2 mm/yr at ~59°E [e.g., *Vernant et al.*, 2004; *Reilinger et al.*, 2006]. The ongoing deformation is principally

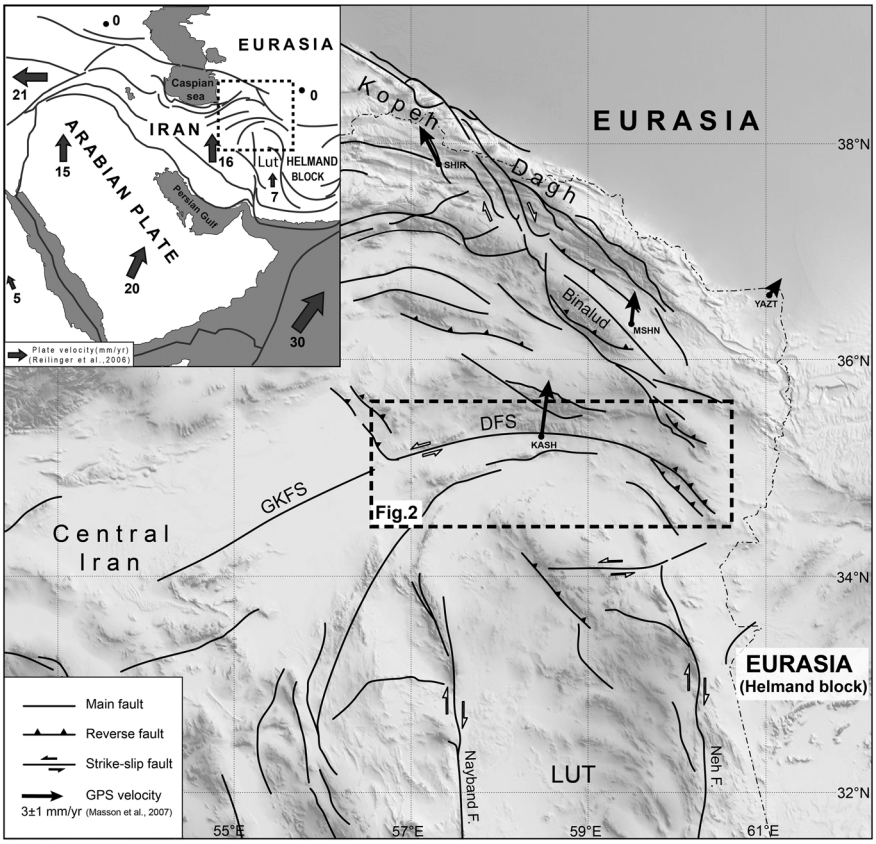

Figure 1. Location of the Doruneh Fault System (DFS) in the Iranian plateau, together with principal structural units overlain on GTOPO30 shaded relief image. Black lines are faults after *Hessami et al.* [2003], *Shabanian et al.* [2010], and *Farbod et al.* [2011]. Black arrows are GPS-derived horizontal velocities (mm/yr) from *Masson et al.* [2007] in a Eurasia-fixed reference frame. The box in the upper left inset shows the location in the Arabia-Eurasia collision zone. Grey arrows and associated numbers represent Arabia-Eurasia plate velocities (mm/yr) after *Reilinger et al.* [2006]. GKFS is the Great Kavir Fault System.

taken up by strike-slip faulting [e.g., *Talebian and Jackson*, 2002; *Walker and Jackson*, 2004; *Regard et al.*, 2005; *Authemayou et al.*, 2006; *Ritz et al.*, 2006a; *Le Dortz et al.*, 2009; *Shabanian et al.*, 2009b; *Farbod et al.*, 2011; *Solaymani Azad et al.*, 2011; *Rizza et al.*, 2013; *Calzolari*, 2015; *Calzolari et al.*, 2015]. Shortening is currently localized in the Zagros (5–9 mm/yr) [*Hessami et al.*, 2006; *Authemayou et al.*, 2009] and Alborz Mountains (~7 mm/yr) [*Djamour et al.*, 2010; *Shabanian et al.*, 2012a; *Mousavi et al.*, 2013].

In Central Iran, the DFS separates the lithospheric north trending dextral strike-slip faults, like the Nayband and Neh faults to the south, from the NW trending Binalud and Kopeh Dagh deformation domains to the north (Figure 1). The DFS separates the pre-Oligocene paleoreliefs to the north (~2500 m elevation) from the Neogene folded rocks armored by Quaternary deposits (~1200 m elevation) to the south (Figure 2). The south sloping Quaternary piedmont is covered by series of alluvial fans, mostly affected by the DFS.

The DFS comprises a western (WFZ), a central (CFZ), and an eastern (EFZ) fault zones (Figure 2) having distinct structural, geomorphic, and kinematic characteristics. The CFZ is pure left-lateral strike slip, while the WFZ is reverse left-lateral oblique-slip. The EFZ is predominantly reverse dip slip. These three fault zones accommodate part of the northward motion between Central Iran and Eurasia in different ways that range from pure compression to the partitioning of deformation on parallel strike-slip and reverse faults (i.e., strain partitioning) [*Farbod et al.*, 2011].

3. Cumulative Left-Lateral Offsets Along the Doruneh Fault System

The surface trace of the DFS is marked by geomorphic features such as Quaternary alluvial fans and their associated drainage system that have been laterally and/or vertically offset along the whole length of the

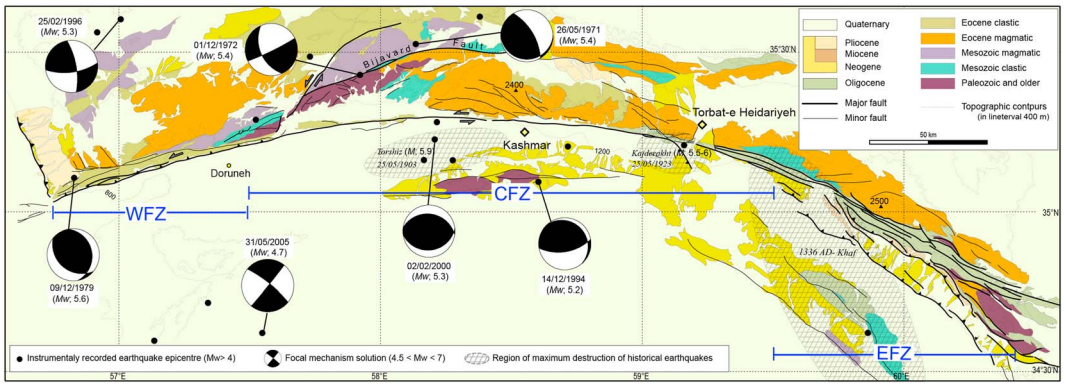

Figure 2. Geological map of the region affected by the DFS simplified after *Eftekhar-Nezhad et al*. [1976] and *Alavi-Naini et al*. [1992]. Fault traces are based on geomorphic and structural mapping by *Farbod et al*. [2011]. WFZ, Western Fault Zone; CFZ, Central Fault Zone; and EFZ, Eastern Fault Zone. Focal mechanisms are mainly taken from the Harvard catalog (http://www.globalcmt.org/CMTsearch.html) and *Jackson and McKenzie* [1984]. Epicenters are from the ISC—EHB Bulletin (Internatl. Seis. Cent., Thatcham, United Kingdom, 2009—http://www.isc.ac.uk). The regions of maximum destruction are based on *Ambraseys and Melville* [1982].

DFS. Detailed geomorphic mapping based on SPOT-5 satellite images complemented by field observations allowed us to identify and to map at the regional scale three successive generations of alluvial fans, which form the inset Q3, Q2, and Q1 regional geomorphic surfaces, from upper to lower elevation and consequently from older to younger age, respectively. All alluvial fans have formed at nearly same geographic latitude over a longitudinal distance of less than 300 km and consequently within a similar desertic climate regime [e.g., *Djamali et al*., 2011].

The measurement and analysis of 18 geomorphic offsets recorded by these surfaces allowed *Farbod et al*. [2011] to characterize along-strike variations in the kinematics of the fault system in a way that the cumulative geomorphic offsets observed along the WFZ and CFZ imply the respective oblique-slip (reverse left lateral) and strike-slip (left lateral) characters of faulting, whereas within the EFZ offsets are principally vertical (reverse).

In order to complete the study by *Farbod et al*. [2011], we used high-resolution (resampled pixel size of 50 cm) GeoEye© images (Google Earth) to create a new data set of cumulative offsets measured in 67 sites that are distributed along the DFS (Table 1). In this study we focus on the left-lateral offsets which only occurred along the WFZ and CFZ. Left-lateral offsets recorded by alluvial fan morphologies (fan shape), associated streams and/or terrace risers between two successive (Q1/Q2 or Q2/Q3) alluvial fan surfaces, were reconstructed (Figure 3a and Table 1). Regarding to the degree of preservation of the Quaternary landforms, we were able to measure 7, 24, and 36 offsets recorded within Q3, Q2, and Q1 surfaces, respectively (Figure 3b and Table 1). We attributed quality criterion, taking into account of both the degree of preservation and the observation quality of the Quaternary landforms (see caption Table 1).

Detailed analysis of Q3 surfaces in seven sites led us to characterize the overall distribution of left-lateral displacements along the CFZ. The maximum offset of 840 ± 70 m in the midlength of this fault zone decreases to ~160 m at both ends (Figure 3b). In the southern side of the WFZ, there are no corresponding surfaces for Q3 alluvial fans allowing such an offset measurement.

The 24 offsets of the Q2 fans and related landforms provided a displacement pattern similar to that deduced from the Q3 offsets along the CFZ (Figure 3b). The CFZ, with the maximum offset of ~300 m, is characterized by larger left-lateral displacement relative to the WFZ. A drastic decrease in offset amounts, from ~140 to ~70 m, occurred at the boundary between the two fault zones. This important variation in offset values may be characteristic of the fault segment maturity; the WFZ can be younger than the CFZ. However, the low density of measurements along WFZ precludes any further interpretation (Figure 3b).

The 36 cumulative offsets recorded by Q1 related features give a complete image of the slip distribution along the fault zones. The ~16 m maximum offset along the WFZ contrasts with the ~60 m offset measured along the CFZ (Figure 3b). Between the longitudes of 58.400°E and 58.442°E, the mountain front is marked by

Table 1. Detailed Characteristics of the Cumulative Left-Lateral Offsets Measured Along the DFS[a]

Site Number	Longitude (°E)	Latitude (°N)	Geomorphic Surface	Offset (m)	Piercing Point and Remarks	Quality
1	56.749	35.032	Q1	0	Western fault termination	A
3	57.082	35.129	Q1	16 ± 4	Fan apex	A
4	57.317	35.177	Q1	15 ± 3	Fan border and incising streams	A
5	57.44	35.201	Q1	12 ± 2	Q1 fan apex	A
8	57.473	35.206	Q1	25 ± 5	Streams incising on the Q1 fan-fan borders	D
9	57.481	35.207	Q1	15 ± 5	Streams incising on the Q1 fan-fan borders	C
12	57.5	35.209	Q1	29 ± 5	Fan shape—drainages	A
13	57.507	35.212	Q1	20 ± 10	Fan shape—individual stream	B
14	57.519	35.213	Q1	27 ± 6	Streams incising the fan	A
18	57.558	35.220	Q1	18 ± 4	Incised streams	B
20	57.58	35.225	Q1	13 ± 3	Streams and small Q1 fans	C
21	57.582	35.225	Q1	14 ± 2	Q1/Q2 riser	B
23	57.615	35.236	Q1	25 ± 3	Incising streams, Q1 fan axial stream	D
24	57.864	35.276	Q1	50 ± 20	Q1 incising streams, Q1/Q0 riser	C
25	58.145	35.294	Q1	55 ± 5	Western fan border and main stream	A
26	58.165	35.297	Q1	65 ± 15	Eastern and western fan border	A
28	58.233	35.297	Q1	40 ± 10	Q1/Q2 riser—stream—fan border	A
30	58.269	35.297	Q1	25 ± 5	Fan border	C
32	58.282	35.297	Q1	30 ± 10	Fan border	B
35	58.304	35.295	Q1	50 ± 10	Eastern and western border of Q1 fan	A
36	58.318	35.295	Q1	60 ± 20	Eastern fan border—one stream	C
37*	58.338	35.295	Q1	60 ± 10	Q1/Q2 riser—streams	A
40	58.38	35.289	Q1	40 ± 10	General reconstruction of borders of two Q1 fans	D
41	58.395	35.288	Q1	10 ± 2	Border of Q1 fan	C
42	58.4	35.287	Q1	0	No faulting in Q1 surfaces	A
43	58.442	35.286	Q1	0	No faulting in Q1 surfaces	A
44	58.443	35.286	Q1	13 ± 3	general morphology of a Q1 fan	C
45	58.46	35.287	Q1	17 ± 2	Q1 ridge—riser—overall geomorphology	B
46	58.5	35.286	Q1	27 ± 10	Risers—eastern border—eastern river—a kariz well	B
47	58.549	35.285	Q1	25 ± 5	Fan morphology—series of streams	B
50*	58.66	35.278	Q1	60 ± 10	Q1/Q2 riser—minimum offset in Q2 streams	A
52	58.76	35.271	Q1	55 ± 5	Incising streams—fan border	A
53	58.764	35.271	Q1	55 ± 5	Main streams incising the fan	B
55	58.873	35.261	Q1	60 ± 10	Pull-apart—western fan border—stream—eastern cultivated depression	B
57	58.926	35.252	Q1	40 ± 10	Overall fan shape and streams reconstruction	D
60	58.954	35.248	Q1	40 ± 5	Overall reconstruction of streams	A
62*	59.009	35.242	Q1	50 ± 10	Q1/Q2 riser	C
69	59.497	35.127	Q1	0	Eastern termination of CFZ	A
1	56.749	35.032	Q2	0	Western fault termination	A
2*	56.766	35.038	Q2	25 ± 5	Eastern fan border	B
6*	57.44	35.201	Q2	60 ± 10	Q2 fan apex	A
7	57.454	35.204	Q2	50 ± 10	Fans—feeding streams	B
11*	57.496	35.205	Q2	70 ± 10	Fan morphology—streams	C
15	57.528	35.214	Q2	90 ± 30	Streams	B
16	57.537	35.215	Q2	100 ± 20	Streams incising Q2—fan morphology	A
17	57.549	35.217	Q2	110 ± 30	Streams incising Q2	D
19	57.571	35.223	Q2	130 ± 15	Fan borders—incising streams	A
22*	57.584	35.226	Q2	140 ± 40	Fan border—apex—feeding stream	A
27	58.194	35.298	Q2	230 ± 20	Two drainage basins in Q3 or older—main river—general Q2 shape	C
29*	58.245	35.297	Q2	190 ± 20	Q2 fan morphology—incising streams	A
31	58.271	35.297	Q2	200 ± 70	Q2 fan border and apex—axial stream	C
33	58.284	35.297	Q2	220 ± 70	Isolated Q2 fan, incising streams	A
38*	58.343	35.295	Q2	200 ± 50	Incising stream	A
39	58.373	35.291	Q2	180 ± 20	Incising and beheaded streams	B
48	58.553	35.284	Q2	300 ± 50	Fan apex—border and feeding stream	A
51	58.669	35.278	Q2	300 ± 50	Eastern fans border—streams-	A
54*	58.855	35.263	Q2	100 ± 20	Fan borders—Incising stream	A
58	58.932	35.251	Q2	210 ± 20	General reconstruction of drainage—overall shape	D
61	58.965	35.247	Q2	190 ± 30	Abandoned and beheaded streams in Q2	B
63	59.009	35.242	Q2	190 ± 30	Abandoned and beheaded streams in Q2	B

Table 1. (continued)

Site Number	Longitude (°E)	Latitude (°N)	Geomorphic Surface	Offset (m)	Piercing Point and Remarks	Quality
64*	59.049	35.235	Q2	210 ± 50	Overall form and incising streams	C
66	59.131	35.22	Q2	170 ± 50	Eastern border—main bordering stream of Q2 fan—Q2/Q3 riser	D
67*	59.323	35.175	Q2	70 ± 20	Western fan border—incising streams	A
69	59.497	35.127	Q2	0	Eastern termination of CFZ	A
1	56.749	35.032	Q3	0	Western fault termination	A
10*	57.492	35.208	Q3	160 ± 100	Streams incising Q3 deposits	D
34	58.29	35.297	Q3	630 ± 70	Streams incising Q3 deposits	D
49	58.57	35.281	Q3	840 ± 70	Fan morphology—main stream	A
56*	58.921	35.253	Q3	330 ± 80	Q3 remnants and incising streams	C
59	58.932	35.251	Q3	350 ± 70	Maximum offset reconstruction of streams (overall shape)	D
65*	59.115	35.222	Q3	290 ± 50	Incising streams in Q3	C
68	59.331	35.174	Q3	170 ± 30	Overall form and incising streams	D
69	59.497	35.127	Q3	0	Eastern termination of CFZ	A

[a]For the location of sites see Figure 3a. The quality criterion indicates the quality level of the offset marker restoration empirically based on the degree of preservation and constraint of the Quaternary offset reconstruction: A, well constrained; B, constrained; C, constrained with more than one possibility; and D, several reconstructions are possible. Asterisks mark the sites in which the offsets presented by *Farbod et al.* [2011] are revised.

a degraded fault scarp line along which remnants of older Q2 and Q3 surfaces are observed on hanging wall of the fault. The fault trace is cover by Q1 and recent alluvial fans such that there is no evidence of faulting at the surface (Figure 4). This relative age relationship between faulting and depositional features reveals an inactive period of faulting according which, since the formation of Q1 surfaces, the CFZ can be divided into two eastern and western segments (see section 5), with symmetrical distribution of lateral displacement with respect to the faulting gap (Figure 3b).

4. Surface Exposure Dating

4.1. Summary of Sampling Strategy and Analytical Procedure for Cosmogenic Dating

Cosmic ray exposure (CRE) dating is based on accumulation of certain cosmogenic nuclides in the surficial materials (few top meters of the crust) exposed to cosmic radiation (see review by *Gosse and Phillips* [2001] and *Dunaï* [2010].

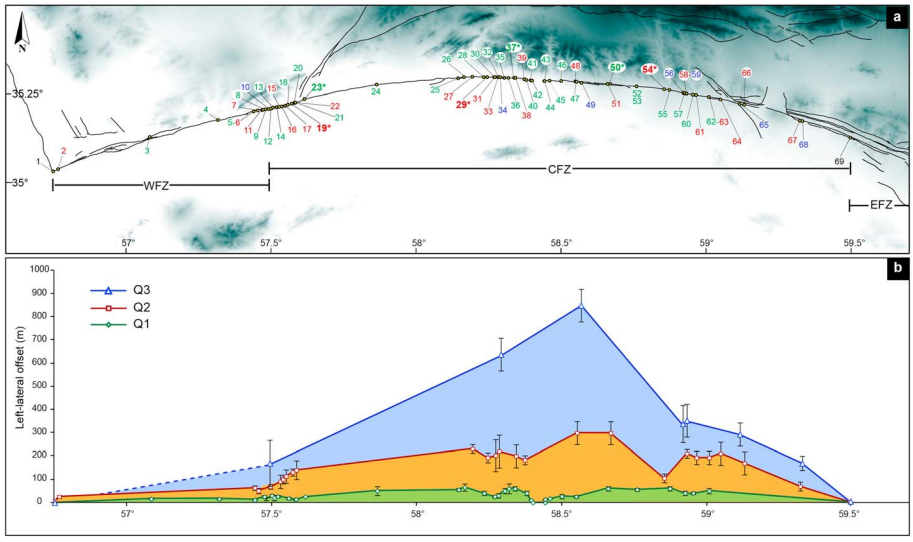

Figure 3. (a) Distribution of the sites in which Quaternary left-lateral offsets were measured along the DFS (Q3 in blue, Q2 in red, and Q1 in green). Details on the cumulative left-lateral offset measurements are given in Table 1 (refer to site numbers). Asterisks mark the sites in which Quaternary surfaces have been dated by ^{36}Cl and ^{10}Be CRE methods. (b) Along-strike variations in cumulative left-lateral offsets recorded by the Q1, Q2, and Q3 fan surfaces. Uncertainties associated to the offset measurements are shown by error bars (see Table 1 for details).

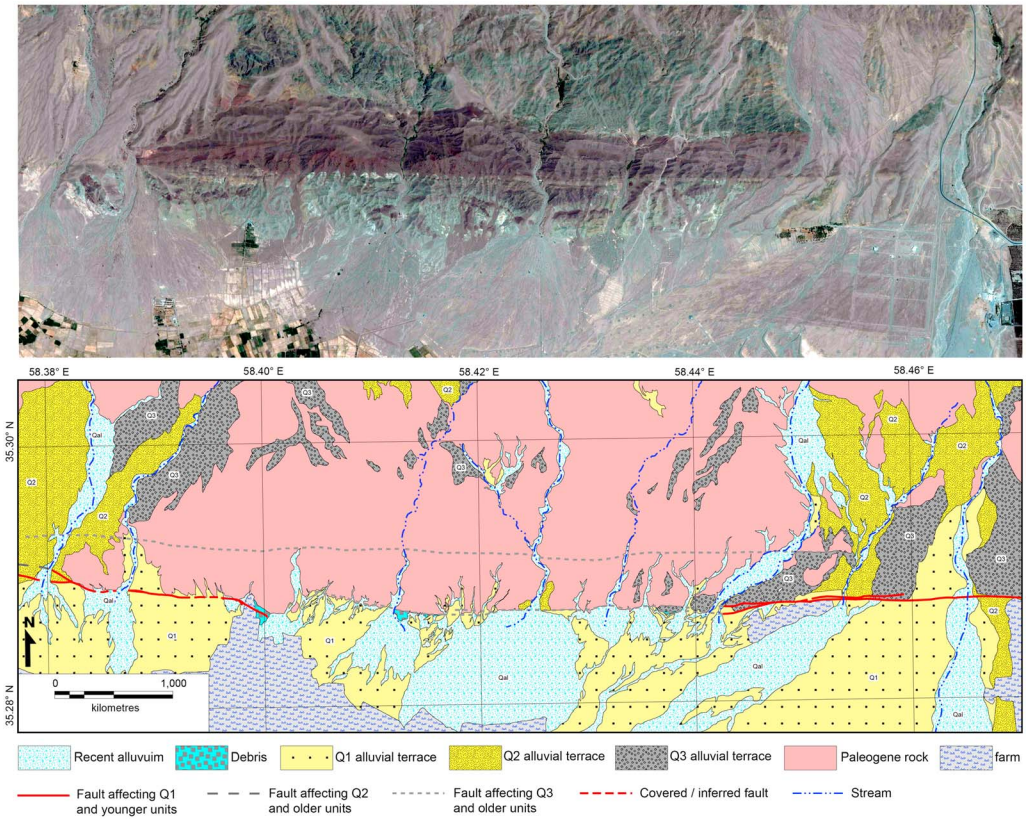

Figure 4. GeoEye satellite image (Google Earth, ©2012 Google, and ©2012 GeoEye) and the related morphotectonic map of the area between 58.400°E and 58.442°E longitudes. The middle part of the area is affected by fault traces cutting Q2 and Q3 alluvial fans and covered by Q1 and younger surfaces. The northern fault strand also affected Q2 and Q3 fan surfaces. Both the western and eastern fault strands clearly cut Q1 and younger alluvial fans.

In order to estimate the CRE ages of alluvial fan surfaces offset along the DFS, we had some difficulties to find well-preserved geomorphic surfaces suitable for dating (in term of lithology) and which were directly affected by faulting. Because the catchment areas of the studied alluvial fans are mostly composed of andesitic rocks, locally intruded by granitic bodies, and rarely of carbonate rocks (Figure 2), the carbonate or quartz-rich clasts necessary for ^{36}Cl and ^{10}Be CRE dating were rare and limited us in the choice of the sampling sites. This precludes sampling large number of surface samples and performing depth-profile sampling.

Instead, based on our geomorphic regional mapping of the three Quaternary surfaces, we dated the well-preserved surfaces wherever it was possible (in term of the lithology) and then correlate the ages of each surface along strike of the DFS. In this way, CRE dating has been done in four sites along the CFZ and two sites along the WFZ, from the concentrations of the in situ-produced ^{10}Be and ^{36}Cl cosmogenic nuclides accumulated in quartz-rich and carbonate rocks, respectively. Despite all difficulties, a total of 36 samples were carefully collected from cobbles 40 × 30 cm (length/wide) in size dispersed on the fan surfaces. The sampled part of the Q1 and Q2 fan surfaces are located away from recent incision rills. Considering the exponential decrease of the ^{36}Cl and ^{10}Be concentrations with depth, the samples were collected from the upper 1–8 cm on top of the cobbles embedded in the surfaces.

Among these 66 samples, only 20 provided enough quartz for analyses. In two sites (10 samples), along the WFZ, catchment areas incised in Cretaceous limestones allowed using the in situ-produced ^{36}Cl cosmogenic nuclide.

The quartz-rich samples were prepared for accelerator mass spectrometry (AMS) ^{10}Be measurements following chemical procedures adapted from *Brown et al.* [1991] and *Merchel and Herpers* [1999], and the carbonate samples were performed following the methodology describe by *Stone et al.* [1996]. All ^{10}Be concentrations are normalized to ^{10}Be/^{9}Be NIST standard reference material 4325 with an assigned value of $(2.79 \pm 0.03)\ 10^{-11}$. The ^{10}Be half-life of $(1.39 \pm 0.01)10^{6}$ years used is that recently recommended by

Table 2. Elemental Composition of the Bulk Rock (%)[a]

Sample	Water	Al_2O_3	Cao	Fe_2O_3	K_2O	MgO	MnO	Na_2O	P_2O_5	SiO_2	TiO_2	Th	U
ANA II-01	0.42	0.348	51.155	0.529	0.055	1.314	0.0137	N.D.	N.D.	3.66	0.027	0.29	1.048
ANA II-02	0.56	0.203	32.72	1.468	0.052	18.807	0.03	N.D.	N.D.	N.D.	0.019	0.13	1.873
ANA II-03	0.39	0.425	33.76	0.22	0.084	18.007	0.008	N.D.	N.D.	0.97	0.033	0.33	1.238
ANA 10-01	0.43	0.236	33.61	0.287	0.048	19.19	0.0121	N.D.	N.D.	N.D.	0.024	0.16	1.858
ANA 10-03	0.41	0.15	31.825	0.663	0.027	19.777	0.0146	N.D.	N.D.	N.D.	0.016	0.10	1.824
ANA 10-04	0.45	0.514	32.21	0.326	0.108	19.223	0.0081	N.D.	N.D.	0.82	0.032	0.37	1.080
ANA 10-06	0.65	0.535	33.96	0.387	0.09	16.563	0.0169	N.D.	N.D.	2.57	0.035	0.40	1.511
DOR-01	0.44	0.135	36.44	0.502	0.022	15.69	0.0117	N.D.	N.D.	N.D.	0.016	0.07	1.081
DOR-02	0.38	0.347	31.685	0.241	0.054	19.39	0.0084	N.D.	N.D.	1.19	0.03	0.21	0.487
DOR-03	0.66	0.173	51.785	0.053	0.027	3.173	0.0099	N.D.	N.D.	N.D.	0.021	0.07	2.884

[a]N.D. is the nondetectable elements.

Korschinek et al. [2010] and *Chmeleff et al*. [2010] according to their two independent measurements. Three chemical blanks prepared with the samples yield $^{10}Be/^{9}Be$ ratio of $1.9 \pm 0.6 \times 10^{-15}$, $2.1 \pm 0.7 \times 10^{-15}$, and $5.3 \pm 2 \times 10^{-15}$. To determine production rates, scaling factors for latitude and altitude corrections were calculated according to *Stone* [2000] and using a modern ^{10}Be spallation production rate at sea level and high latitude of 4.5 ± 0.3 atoms/g-SiO_2/yr to account for the reevaluation of absolute calibration of ^{10}Be AMS standards proposed by *Nishiizumi et al*. [2007].

For the carbonate samples, major elemental compositions of rock samples were determined (Table 2) using inductively coupled plasma-optical emission spectrometry technique at the Centre National de la Recherche Scientifique (Service d'Analyse des Roches et des Minéraux (SARM), CNRS-Nancy). The ages of samples were calculated using the Ca concentration in the dissolved part of the samples according to *Schimmelpfennig et al*.'s [2009] Excel spreadsheet.

For all sampling sites, corrections for shielding by the surrounding topography, snow cover, and sample geometry, following *Dunne et al*. [1999], have negligible impact on the surface production rates. The in situ-produced ^{36}Cl and ^{10}Be concentrations are presented in Tables 2–4. At each sampling site, the distribution of the estimated CRE ages and their associated uncertainties were examined using the sum of the Gaussian probability distributions [e.g., *Deino and Potts*, 1992] according to *Taylor* [1997]:

$$P_{\mathrm{sum}}(t) \sum_{t} e^{-(t-a_t)^2/2\sigma_i^2} / \sigma_i \sqrt{2\pi}, \tag{1}$$

where t is time, a_i is the exposure age of sample i, and $(2\sigma_i)$ is the associated uncertainty. The probability of 95%, i.e., 2σ, was chosen to calculate uncertainties associated with exposure ages:

$$\sigma^2 = 1(N-1) \sum_{i=1}^{i=N} (t_1 - \bar{t})^2. \tag{2}$$

Table 3. Sample Characteristic and ^{36}Cl Exposure Ages[a]

Sample	Surface	Latitude (°N)	Longitude (°E)	Elevation (m)	Cao (%)	Chlorine (ppm)	^{36}Cl Production Rate (atom/g/yr)	^{36}Cl (10^6atom/g)	Age (ka)		
									Zero Erosion	1 m/Ma	7 m/Ma
ANAII-01	Q2	35.24	57.61	972	54.25	80	46.86	1.66 ± 0.11	38.3 ± 4.2	38.6 ± 4.2	-
ANAII-02	Q2	35.24	57.61	973	32.25	119	35.56	1.50 ± 0.11	41.3 ± 4.7	40.6 ± 4.4	-
ANAII-03	Q2	35.24	57.61	973	32.91	104	34.92	1.42 ± 0.09	40.6 ± 4.4	40.1 ± 4.4	-
ANA10-01	Q3	35.24	57.61	1001	33.89	111	36.43	1.59 ± 0.12	42.4 ± 4.8	-	41.4 ± 4.5
ANA10-03	Q3	35.24	57.61	1000	31.27	269	56.72	3.85 ± 0.34	70.2 ± 9.0	-	61.8 ± 6.7
ANA10-04	Q3	35.24	57.61	1004	30.79	133	36.01	2.78 ± 0.2	77.3 ± 9.0	-	79.0 ± 8.6
ANA10-06	Q3	35.24	57.61	999	35.88	92	35.41	3.23 ± 0.2	98.2 ± 11.1	-	130.3 ± 14.3
DOR-01	Q3	35.23	57.57	990	34.53	117	37.44	2.65 ± 0.19	74.3 ± 6.8	-	76.5 ± 8.4
DOR-02	Q3	35.23	57.57	993	32.82	129	37.67	3.41 ± 0.26	96.1 ± 11.5	-	100.8 ± 11.1
DOR-03	Q3	35.23	57.57	1005	53.32	35	42.52	2.7 ± 0.12	70.2 ± 7.6	-	100.3 ± 11

[a]In situ-produced ^{36}Cl concentration and modeled ages of samples. The CRE ages, from left to right, are calculated assuming: no denudation, the denudation rate of 1 m/Ma reported for the well-preserved alluvial fan in Central Iran [*Le Dortz et al*., 2011], and a maximum possible denudation rate of 7 m/Ma estimated for the most eroded Nay Q3 fan surface. The rejuvenation of some sample ages is explained by the high quantity of natural chlorine in the samples.

Table 4. Sample Characteristics and ^{10}Be Exposure Ages[a]

Sample	Surface	Longitude (°E)	Latitude (°N)	Elevation (m)	^{10}Be Production Rate (atoms/g-SiO_2/yr)	^{10}Be (Atom/g-SiO_2)	Age (ka)	
							Zero Erosion	1 m/Ma
KHA 07-2	Q1	58.335	35.294	1099	9.6767	136221 ± 20923	13.8 ± 2.1	14 ± 2.14
KHA 07-3	Q1	58.337	35.293	1102	9.6983	113362 ± 7388	11.5 ± 0.7	11.6 ± 0.7
KHA 07-6	Q1	58.337	35.293	1101	9.6910	216499 ± 14747	22 ± 1.6	22.4 ± 1.5
KHA 07-7	Q1	58.338	35.293	1102	9.6983	255471 ± 22321	26 ± 2.3	26.5 ± 2.3
AZ II-03	Q1	58.839	35.263	1316	11.3627	246699 ± 11897	21.4 ± 1.0	21.7 ± 1.0
AZ II-04	Q1	58.839	35.264	1320	11.3964	257468 ± 13338	22.2 ± 1.1	22.6 ± 1.2
AZ II-05	Q1	58.839	35.264	1320	11.3964	192020 ± 8701	16.5 ± 0.7	16.8 ± 0.7
AZ II-06	Q1	58.839	35.264	1320	11.3964	156048 ± 12382	13.4 ± 1.1	13.6 ± 1.1
AZ II-07	Q1	58.839	35.264	1320	11.3964	287008 ± 8538	24.8 ± 0.7	25.3 ± 0.7
AZ 10-01	Q2	58.854	35.275	1385	11.9551	527182 ± 15858	43.6 ± 1.3	45.2 ± 1.4
AZ 10-03	Q2	58.854	35.275	1383	11.9378	359963 ± 12688	29.7 ± 1.0	30.4 ± 1.1
AZ 10-08	Q2	58.854	35.276	1389	11.9905	328054 ± 10746	26.9 ± 0.9	27.5 ± 0.9
AZ 10-09	Q2	58.854	35.276	1390	11.9992	609639 ± 18122	50.3 ± 1.5	52.40 ± 1.5
MAZ 07-2	Q2	58.239	35.295	1071	9.4753	331413 ± 43584	34.5 ± 4.5	35.5 ± 4.6
MAZ 07-4	Q2	58.239	35.294	1067	9.4465	502841 ± 46495	52.8 ± 4.9	55.0 ± 5.1
MAZ 07-6	Q2	58.239	35.294	1065	9.4322	329875 ± 20871	34.5 ± 2.2	35.5 ± 2.2
MAZ 07-7	Q2	58.239	35.295	1058	9.3828	337368 ± 64936	35.5 ± 6.8	36.5 ± 7.0
ESM 07-3	Q2	58.666	35.275	1345	11.6103	209169 ± 20816	17.7 ± 1.7	18.0 ± 1.78
ESM 07-6	Q2	58.664	35.274	1334	11.5167	586977 ± 31640	50.5 ± 2.7	52.6 ± 2.8
ESM 07-9	Q3	58.6731	35.281	1361	11.7488	1204036 ± 45597	102.8 ± 3.9	-

[a]In situ-produced ^{10}Be concentration and modeled ages of the surface sample from the six alluvial fans offset by DFS. ^{10}Be concentrations analytical uncertainties (reported as 1σ) include a conservative 0.5% external uncertainty based on long-term measurements of standards, a 1 sigma statistical error on counted ^{10}Be events and the uncertainty associated with the chemical blanks correction [*Arnold et al.*, 2010]. The samples collected from the Nay alluvial fan are named by ESM. The CRE ages are calculated assuming no denudation (left hand), and the maximum denudation rate of 1 m/Ma reported for the well-preserved alluvial fan in Central Iran [*Le Dortz et al.*, 2011].

The chi-square inversion test [*Ward and Wilson*, 1978] has also been used to control the differences between modeled and measured concentration.

4.2. Cosmogenic Dating Results

In this study, the determination of minimum exposure ages (Tables 2 and 4) relies on the assumption that the effects of erosion on the most preserved part of the alluvial surfaces (i.e., sampled parts) and cosmogenic nuclide inheritance from exposure prior to the deposition of clasts are negligible. Two other sets of exposure ages were calculated using maximum denudation rates of 1 m/Ma and 7 m/Ma (maximum possible denudation rate on the oldest abandonment fan surfaces) allowing us to determine upper and lower bounds for the surface abandonment ages (Tables 3 and 4 and see section 4.3).

4.2.1. ^{10}Be CRE Ages From Q1 Surfaces

To verify the simultaneous abandonment of the Q1 surfaces, two Q1 surfaces were sampled at two ~45 km apart localities along the CFZ (Figures 3a and 5). At the first site (Azghand) five samples were analyzed from quartz-rich granite and granodiorite clasts embedded in the fan surface (Figure 5a). The samples from the Azghand surface yield CRE ages ranging from 13.4 ± 1 to 24.8 ± 0.7 ka (Table 4). The Gaussian age probability distribution (P_{sum}) of these samples provides evidence for two populations; they are ranged from ~13 to ~16 ka and from ~21 to ~24 ka, respectively (Figure 5c). At the second site (Khalilabad, Figure 5b), among the collected quartz-rich granitic cobbles, we analyzed four samples that yielded CRE ages ranging from 11.5 ± 0.7 to 26 ± 2.3 ka (Table 4). The probability distribution also shows two populations of ages ranged from ~11 to ~14 ka and from ~22 to ~26 ka, respectively (Figure 5d). The similar age distribution confirms that these both Q1 surfaces are coeval, with the same complexity in the exposure history as shown by the bimodal age distribution (see section 4.3).

4.2.2. ^{10}Be and ^{36}Cl CRE Ages From Q2 Surfaces

The Q2 surface was sampled in four localities along the CFZ and WFZ (Figure 3a). Those are Azghand, Nay, Mazdeh (quartz-rich samples for ^{10}Be dating), and Anabad (carbonate samples for ^{36}Cl dating) alluvial fan surfaces (Figure 6).

Four samples from andesitic clasts embedded in the Azghand Q2 fan surface (Figure 6a) yield ^{10}Be CRE ages ranging from 26.9 ± 0.9 to 50.3 ± 1.5 ka (Table 4). Their probability distribution displays evidence for two distinct age populations ranged from ~27 to ~30 ka and 43.6 ± 1.3 to 50.3 ± 1.5 ka (Figure 6d), respectively.

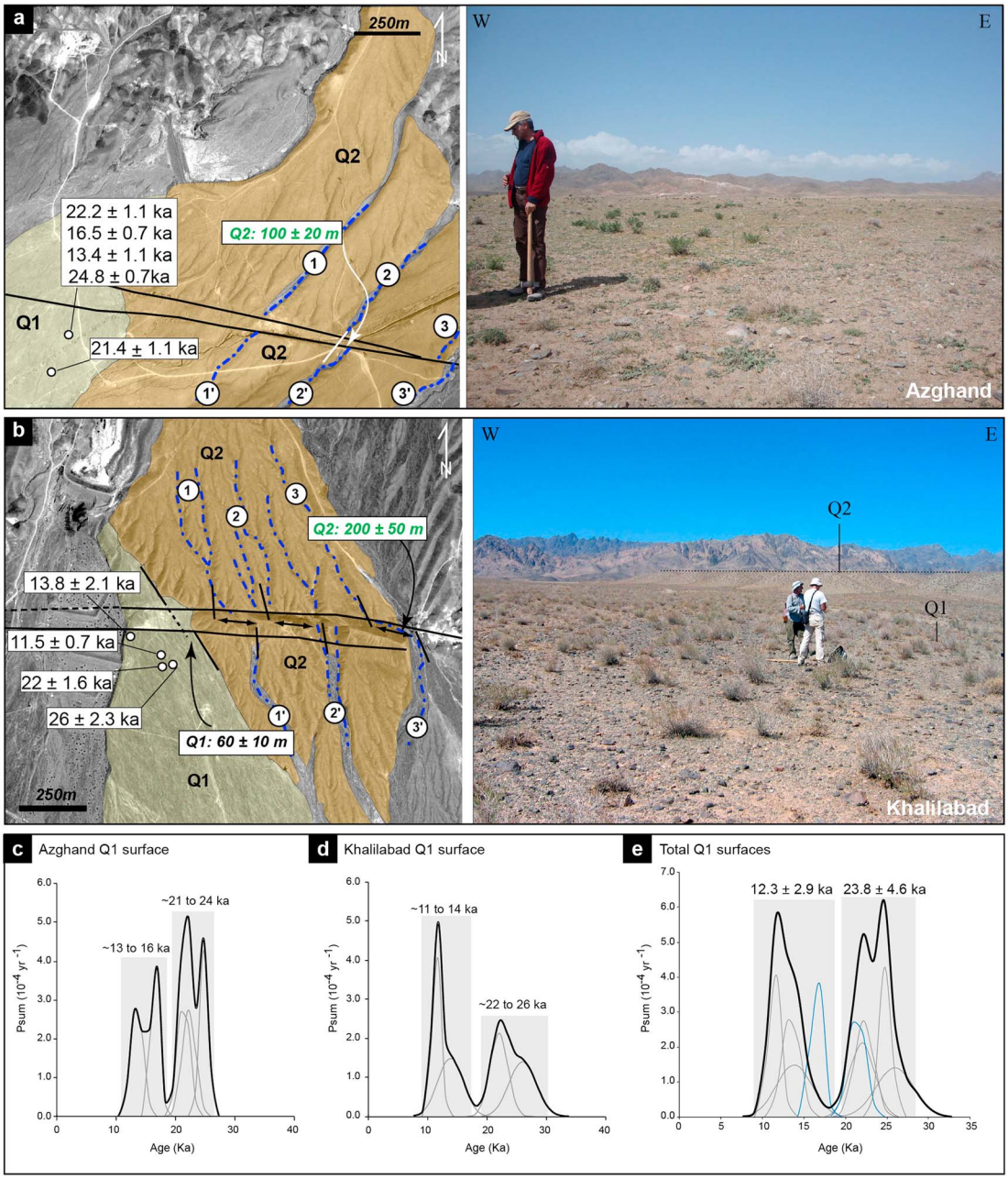

Figure 5. (a) Azghand and (b) Khalilabad Q1 fan surfaces. Figures 5a and 5b (left) show the geomorphologic interpretation of Quaternary inset fan surfaces (GeoEye images—Google Earth). White circles show the position of the surface sampling. Labels are the ^{10}Be CRE ages as presented in Table 4. Other white boxes are offset values recorded by the fan surfaces. Figures 5a and 5b (right) are the field photograph of the sampled part of the Q1 fan surfaces. (c and d) The age probability distributions of ^{10}Be exposure ages for the fan surfaces. The thick curve is the sum of the Gaussian distribution of sample ages. Thin grey curves represent the age probability for each individual sample. (e) Age probability distribution of all Azghand and Khalilabad samples, showing two age populations. Weighted mean ages of 12.3 ± 2.9 and 23.8 ± 4.6 ka are derived for each population. The thin blue curve represents the age rejected in chi-square test. A conservative uncertainty (2σ) is associated to the abandonment ages.

Seven samples were collected on the Nay Q2 surface, ~17 km west of the Azghand Q2 alluvial fan. Only two samples have provided quartz mass amounts allowing ^{10}Be dating (Figure 7a). They yield CRE ages of 17.7 ± 1.7 and 50.5 ± 2.7 ka, the latter being coherent with the maximum CRE age estimates at the Azghand site. Farther west, on the Mazdeh fan surface (Figure 6b), the ^{10}Be CRE ages deduced from the four andesitic samples, ranged from 34.5 ± 2.2 to 52.8 ± 4.9 ka (Table 4), are within the range of those obtained on the Azghand Q2 surface.

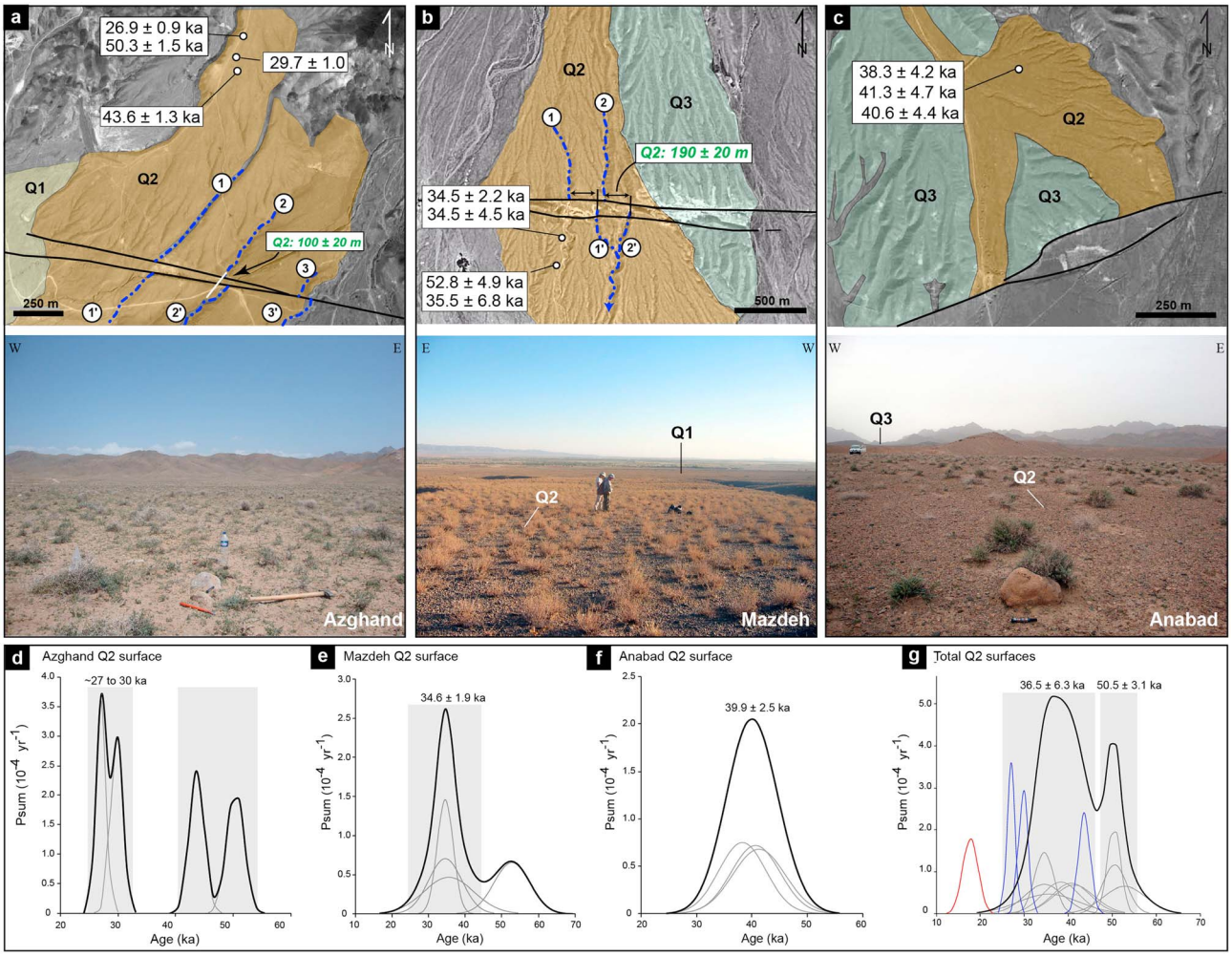

Figure 6. (a) Azghand, (b) Mazdeh, and (c) Anabad sampling sites. Figures 6a–6c are the geomorphic interpretations of the sampled Q2 fan surfaces (GeoEye images—Google Earth). Field photographs of the surfaces are shown in Figures 6a–6c. The age probability distribution of the (d) CRE, (e) ^{10}Be, and (f) ^{36}Cl ages. (g) Age probability distribution of all ^{10}Be and ^{36}Cl samples showing two populations of exposure ages. The weighted mean ages of 36.5 ± 6.3 and 50.5 ± 3.1 ka are calculated. The thin red curve represents the outlier sample. See the caption of Figure 5 for more details.

The probability distribution of these four dated samples provides evidence for a sharp peak at 34.6 ± 1.9 ka distinct from the 52.8 ± 4.9 ka oldest CRE age (Figure 6e). Finally, in the westernmost Q2 fan surface at Anabad, three selected carbonate clasts yield a ^{36}Cl CRE ages ranged from 38.3 ± 4.2 to 41.3 ± 4.7 ka. The probability distribution shows a single sharp peak at 39.9 ± 2.5 ka (Figures 6c and 6f).

The sum of the Gaussian probability distribution of the 13 ^{10}Be and ^{36}Cl CRE ages obtained on the Q2 surfaces is clearly bimodal, considering the ESM07-3 CRE age (17.7 ± 1.7 ka) as an outlier (Figure 6g). The first CRE age population ranges from ~27 to ~43 ka, while the second CRE age population clustered around ~50 ka. Such a bimodal age distribution, regardless the age values, is similar to that obtained from the Q1 surfaces (section 4.2.1) and confirms the complex exposure history of the clasts (see section 4.3 for the CRE ages discussion).

4.2.3. ^{10}Be and ^{36}Cl CRE Ages From Q3 Surfaces

A total of 16 quartz-rich and carbonate samples were collected from three Q3 alluvial fan surfaces offset along the CFZ and WFZ (Figures 3a and 7). Among five quartz-rich samples found and collected from rare, nearly preserved parts of the Nay Q3 alluvial fan (Figure 7a), only one sample provided the quartz mass amount allowing ^{10}Be dating and yielded a CRE age at 102.8 ± 3.8 ka (Table 4). The four carbonate samples on the Anabad Q3 surface (Figure 7b) yielded ^{36}Cl CRE ages ranging from 42.4 ± 4.8 to 98.2 ± 11 ka, with three CRE ages clustering at 79.8 ± 5.5 ka (Figure 7d). Three samples from the Doruneh Q3 fan surface (Figure 7c) yielded ^{36}Cl CRE ages of 70.2 ± 7.5, 74.2 ± 8.6, and 96.1 ± 11.5 ka, their weighted mean CRE age being 76.7 ± 5.1 ka (Figure 7e).

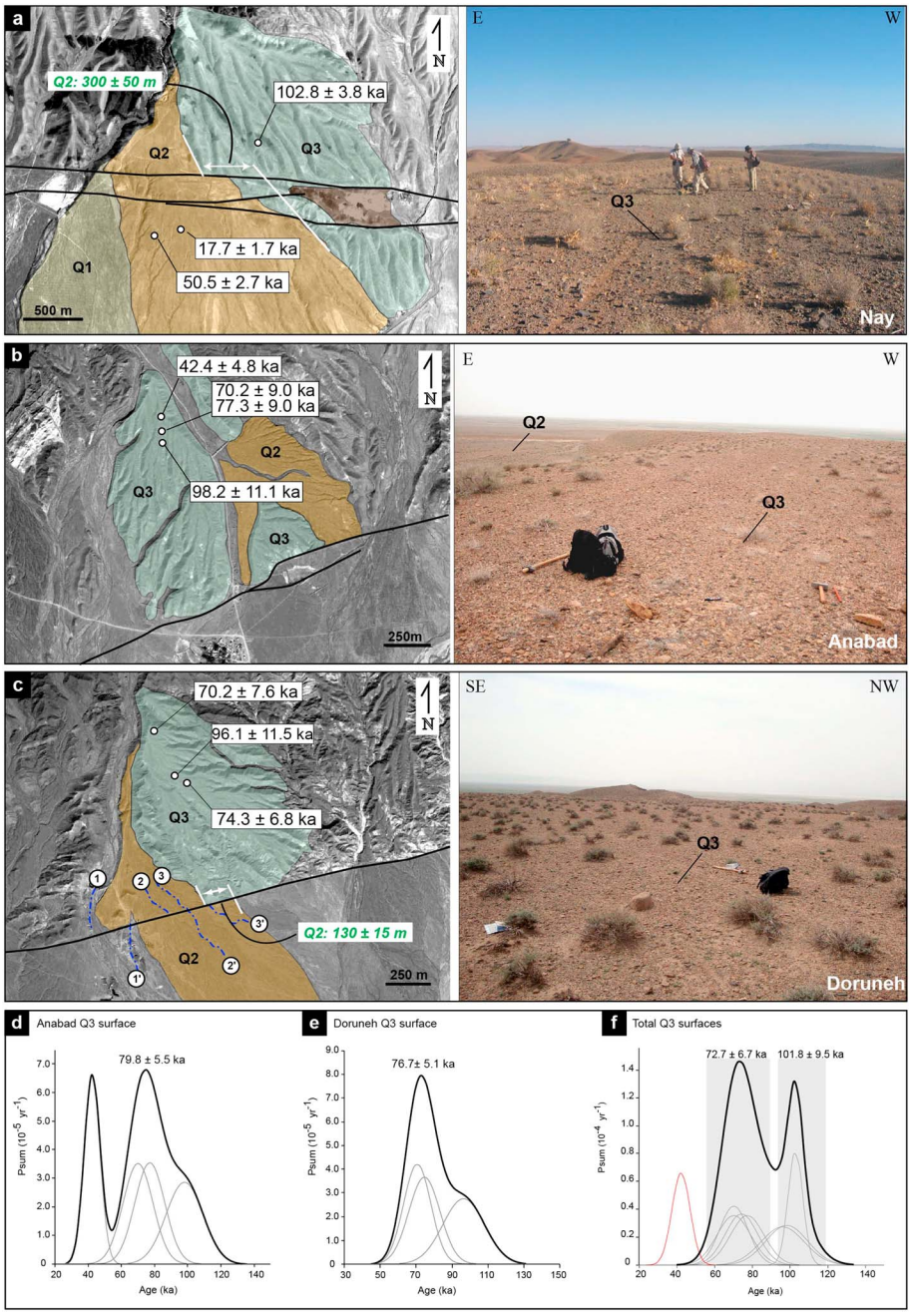

Figure 7. (a) Nay, (b) Anabad, and (c) Doruneh sampling sites (Q3 alluvial surfaces); description is like Figure 6. (d and e) The age probability distribution of Anabad and Doruneh sites. (f) Age probability distribution of all ^{10}Be and ^{36}Cl samples which show two populations of exposure ages. The weighted mean age of 72.7 ± 6.7 and 101.8 ± 9.5 ka are calculated by chi-square test for each population. The thin red curve represents the outlier sample. See the caption of Figure 5 for more details.

The sum of the Gaussian probability distribution of the seven ^{36}Cl and one ^{10}Be CRE ages, considering the CRE age of 42.4 ± 4.8 ka as an outlier, is bimodal providing evidence for two CRE age peaks at 72.7 ± 6.7 and 101.8 ± 9.5 ka, respectively (Figure 7f).

4.2.4. Effects of Erosion and Inheritance on CRE Dating Results

Erosion minimizes CRE ages of surface samples by decreasing cosmogenic isotope concentrations. In a lack of direct erosional features like young gullies and differential erosion on the sampled parts of alluvial surfaces, one may attribute the current position of large clasts to erosion processes which cause upward migration of

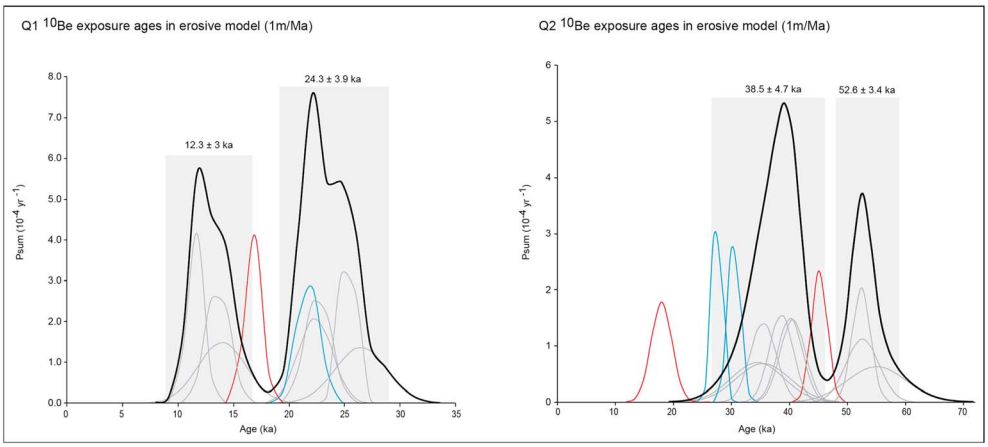

Figure 8. Age probability distribution of the Q1 and Q2 fan surfaces calculated assuming a denudation rate of 1 m/Ma; two populations of exposure ages are recognized on both surfaces. See the caption of Figure 5 for more details.

clasts to the land surfaces [e.g., *Thomas*, 1989; *Cooke et al*., 1993; *Wells et al*., 1995]. In such cases, clasts are concentrated at the land surface at significantly different times, and thus, a random surface sampling (e.g., our strategy) will show considerable scatter in the ages of clasts [e.g., *Bierman*, 1994; *Zreda et al*., 1994; *Phillips et al*., 1997]. In this case, the older age cluster is closer to the true surface abandonment age [e.g., *Zreda et al*., 1994; *Ritz et al*., 1995; *Phillips et al*., 1997; *Brown et al*., 2005]. In contrast, the surface CRE ages calculated for Q1 and Q2 surfaces, although bimodal, are relatively coherent and well clustered indicating that the clasts have stayed at the fan surfaces regardless of erosion processes (if any). The suggestion of low denudation rate on Q1 and Q2 surfaces is likely to be valid; in the southern regions of Central Iran experiencing similar hyper-arid climatic and strike-slip tectonic regimes, *Le Dortz et al*. [2009, 2011] reported a denudation rate lower than 1 m/Ma by analyzing cosmogenic ^{10}Be and ^{36}Cl in surface cobbles and near surface amalgams collected from alluvial fan surfaces (abandoned 10 to 300 ka ago). Moreover, the erosion rate affecting surface cobbles and boulders may be significantly lower than the erosion rate estimated for the corresponding surfaces [e.g., *Ritz et al*., 2006b]. To be more conservative, we calculated two other sets of CRE ages (Tables 3 and 4) using denudation rates of 1 and 7 mm/Ma for the alluvial surfaces (see section 4.3). The maximum denudation rate of ~7 m/Ma is based on the steady state nuclide concentrations in samples collected from the most eroded Q3 surface (Nay alluvial fan).

Conversely to erosion, cosmogenic nuclide inheritance from exposure prior to the deposition of alluvial surfaces leads to exceed the true abandonment age of alluvial surfaces [e.g., *Le Dortz et al*., 2011; *Schmidt et al*., 2011]. Two principal causes of such a high, variable inherited nuclide concentration are complex transport histories and different sources of clasts. Clasts coming from a large catchment area and through a long transport pathway should undergo a complex transport history. This problem would be worse for inset Quaternary terraces, where clasts are detached from upper alluvial surfaces and form lower inset terraces downstream [e.g., *Le Dortz et al*., 2009, 2011; *Schmidt et al*., 2011; *Le Béon et al*., 2010; *Ritz et al*., 2006b]. In the area of interest, the prevailing of these particular geomorphic situations highlights the importance of inheritance in the concentrations of in situ-produced cosmogenic nuclides in our samples (see section 4.3). In this case, the older age population for a given surface overestimates its abandonment age, while the younger age population is most likely closer to true abandonment age of the surface [e.g., *Le Dortz et al*., 2009, 2011].

4.3. Timing of the Abandonment of Q1, Q2, and Q3 Alluvial Surfaces

The CRE age distribution of all the samples collected either on the Q1 or the Q2 fan surfaces shows a bimodal pattern evidencing two CRE age populations for each surface (Figures 5e and 6g). Given the similarity of CRE age patterns for different geomorphic surfaces, the possible cause of this systematic age dispersion could not coming from the sampling (section 4.2.4). Also, there is no geomorphic evidence of multistage clast deposition on the Q1 and Q2 fan surfaces.

For samples from Q1 and Q2 surfaces, two CRE age sets were calculated (section 4.2.4). The ages obtained for 1 m/Ma of denudation are slightly older than those calculated assuming no erosion (section 4.2), while their distributions remain bimodal (Figure 8). Interestingly, for each fan surface, the younger age population,

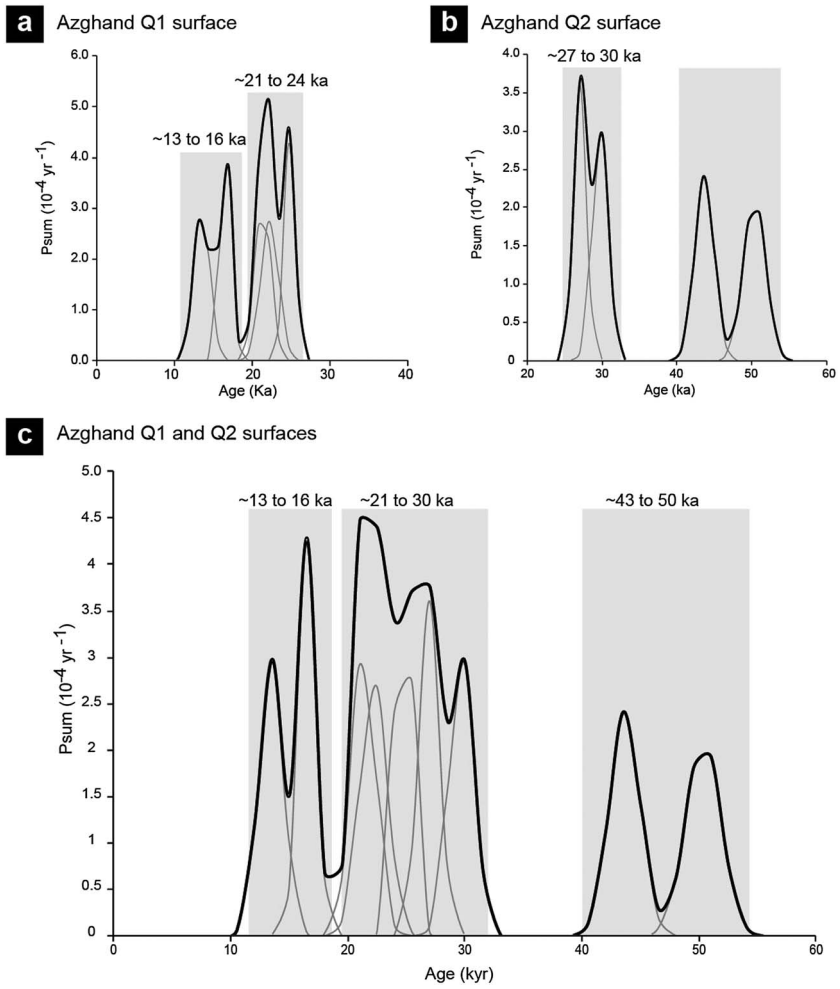

Figure 9. (a) ^{10}Be age probability distribution of Q1 fan surface in Azghand site showing two age populations ranging from ~13 to ~16 ka and ~21 to ~24 ka. (b) ^{10}Be age probability distribution of Q2 abandonment surface in the Azghand site showing an age population between ~27 and ~30 ka and two older ages of 43.6 ± 1.3 and 50.3 ± 1.5 ka. (c) Age probability distribution of both Q1 and Q2 inset abandonment surfaces. See the caption of Figure 5 for more details.

assuming a denudation rate of 1 m/Ma, is still younger than the older age population calculated assuming no erosion. In such a way, denudation rates of ~10 m/Ma (on Q2 surfaces) and ~25 m/Ma (on Q1 surfaces) are necessary to overtake the older age population calculated assuming no erosion. Such denudation rates are most unlikely considering the maximum denudation rate of 1 mm/Ma reported by *Le Dortz et al*. [2009, 2011] and the well-preserved geomorphology of the Q1 and Q2 fan surfaces. This indicates that the bimodal age pattern does not result from surface denudation and the associated upward migration of the clasts to the land surface [e.g., *Thomas*, 1989; *Cooke et al*., 1993; *Wells et al*., 1995].

In the study area, almost all younger alluvial surfaces are inset in older fan surfaces (Q1 in Q2 and Q2 in Q3). The formation of inset alluvial fans during successive deposition/erosion stages could explain the bimodal age distributions. The inset surface pattern allows clasts exposed on upper surfaces to be detached from older alluvial fans due to stream channel incision, gravitational movements, or during occasional flooding periods [e.g., *Le Dortz et al*., 2009, 2011; *Schmidt et al*., 2011; *Le Béon et al*., 2010; *Ritz et al*., 2006b] and to form lower inset surfaces.

We have tested the aforementioned hypothesis comparing CRE ages of clasts embedded in two inset alluvial surfaces; in the Azghand area, two inset Q1 and Q2 alluvial fan surfaces (sections 4.2.1 and 4.2.2) were sampled. The CRE ages for the Q1 clasts show two age populations: the first one is between ~13 and ~16 ka and the second one between ~21 and ~24 ka (Figure 9a). The clasts from the Q2 surface yield ages

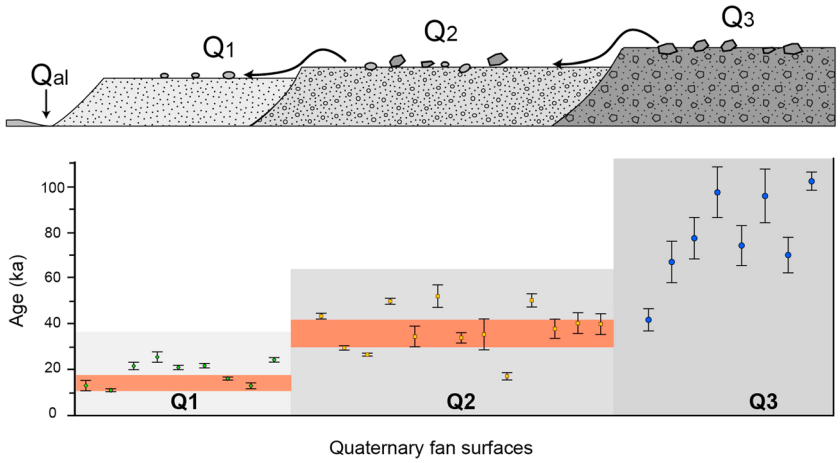

Figure 10. (top) Schematic model for the three inset abandonment surfaces. The clasts of the upper (older) surface could have reworked to the lower (younger) forming surface during the incision of the upper surface by the feeding stream and its tributaries. (bottom) ^{10}Be and ^{36}Cl exposure ages of the three Q1, Q2, and Q3 surfaces. Red boxes correspond to the 2σ uncertainty for the weighted mean ages of Q1 and Q2 surfaces (see Figure 8).

ranging between ~27 and ~30 ka (Figure 9b) and two older ages at 43.6 ± 1.3 and 50.3 ± 1.5 ka (section 4.2.2). The mean CRE age deduced from the Q1 older samples (~23 ka) is similar to the mean CRE age deduced from the Q2 younger samples (~27 ka), suggesting that older samples on the Q1 surface may originate from the Q2 surface. This is also suggested by the sum of the probability distribution of the ages of both Q1 and Q2 samples that shows only three ages populations (Figure 9c).

Accordingly, the inset scenario is retained to explain the bimodal distribution of the alluvial fan surface CRE ages (Figure 10). These results, together with optically stimulated luminescence/infrared stimulated luminescence dating performed along the Doruneh Fault System, which lead to a maximum abandonment age of ~10 ka [*Fattahi et al.*, 2007] for the younger (Q1, this study) abandonment surface, confirm that the younger CRE age populations are most likely closer to true ages of abandonment surface, i.e., the negligible erosion assumption. The exposure ages of 12.3 ± 2.9 and 36.5 ± 6.3 ka (±2σ) are therefore proposed for the Q1 and Q2 alluvial fans, respectively (Figures 8a and 8b).

The bimodal pattern of the CRE age distribution on the Q3 fan surfaces could be explained differently. The absence of alluvial surfaces above the Q3 alluvial surfaces considerably reduces the likelihood of a systematic inheritance in the Q3 samples. On the other hand, as indicated by streams incising their entire surface, the Q3 alluvial fan surfaces underwent denudation rates higher than the Q2 and Q1 surfaces. The degree of preservation, however, varies among Q3 fan surface. As for the Nay Q3 surface (Figure 7a),

Table 5. Left-Lateral Slip Rates Along the DFS Based On Offsets Recorded by Q3 Surfaces[a]

Site Number	Surface	Longitude (°E)	Latitude (N°)	Offset (m)	Minimum Age (ka)	Maximum Age (ka)	Maximum Slip Rate (mm/yr)	Minimum Slip Rate (mm/yr)	Suggested Slip Rate (mm/yr)	Quality
1	Q3	56.749	35.032	0	103 ± 4	130 ± 14	0	0	0	A
10	Q3	57.492	35.208	160 ± 100	103 ± 4	130 ± 14	1.6 ± 1.0	1.2 ± 0.8	1.3 ± 0.9	D
34	Q3	58.29	35.297	630 ± 70	103 ± 4	130 ± 14	6.1 ± 0.7	4.8 ± 0.7	5.3 ± 1.1	D
49	Q3	58.57	35.281	840 ± 70	103 ± 4	130 ± 14	8.3 ± 0.8	6.5 ± 0.9	7.1 ± 1.3	A
56*	Q3	58.921	35.253	330 ± 80	103 ± 4	130 ± 14	3.2 ± 0.8	2.5 ± 0.7	2.8 ± 0.8	D
59*	Q3	58.932	35.251	350 ± 70	103 ± 4	130 ± 14	3.4 ± 0.7	2.7 ± 0.6	2.9 ± 0.8	D
65*	Q3	59.115	35.222	290 ± 50	103 ± 4	130 ± 14	2.8 ± 0.5	2.2 ± 0.5	2.4 ± 0.6	C
68*	Q3	59.331	35.174	170 ± 30	103 ± 4	130 ± 14	1.7 ± 0.3	1.3 ± 0.3	1.4 ± 0.3	C
69	Q3	59.497	35.127	0	103 ± 4	130 ± 14	0	0	0	A

[a]Suggested slip rates are based on the age of 120 ± 20 ka inferred for the abandonment of Q3 surfaces (section 4.2.4). Asterisk marks the sites in which the assignment of offset markers to weighted mean ages determined for the Q1, Q2, and Q3 fan generations is not straightforward.

Table 6. Left-Lateral Slip Rates Along the DFS Based On Offsets/Ages of Q1 and Q2 Surfaces[a]

Site Number	Surface	Longitude (°E)	Latitude (N°)	Offset (m)	Age (ka)	Slip Rate (mm/yr)	Quality
1	Q2	56.749	35.032	0	36.5 ± 6.3	0	A
2	Q2	56.766	35.038	25 ± 5	36.5 ± 6.3	0.7 ± 0.2	B
6	Q2	57.44	35.201	60 ± 10	36.5 ± 6.3	1.6 ± 0.4	A
7	Q2	57.454	35.204	50 ± 10	36.5 ± 6.3	1.4 ± 0.4	B
11	Q2	57.469	35.205	70 ± 10	36.5 ± 6.3	1.9 ± 0.4	C
15	Q2	57.528	35.214	90 ± 30	36.5 ± 6.3	2.5 ± 0.9	B
16	Q2	57.537	35.215	100 ± 20	36.5 ± 6.3	2.7 ± 0.7	A
17	Q2	57.549	35.217	110 ± 30	36.5 ± 6.3	3.0 ± 1.0	D
19	Q2	57.571	35.223	130 ± 15	36.5 ± 6.3	3.6 ± 0.7	A
22	Q2	57.584	35.226	140 ± 40	36.5 ± 6.3	3.8 ± 1.3	A
27	Q2	58.194	35.298	230 ± 20	36.5 ± 6.3	6.3 ± 1.2	C
29	Q2	58.245	35.297	190 ± 20	36.5 ± 6.3	5.2 ± 1.1	A
31	Q2	58.271	35.297	200 ± 70	36.5 ± 6.3	5.5 ± 2.1	C
33	Q2	58.284	35.297	220 ± 70	36.5 ± 6.3	6.0 ± 2.2	A
38	Q2	58.343	35.295	200 ± 50	36.5 ± 6.3	5.5 ± 1.7	A
39	Q2	58.373	35.291	180 ± 20	36.5 ± 6.3	4.9 ± 1.0	B
48	Q2	58.553	35.284	300 ± 50	36.5 ± 6.3	8.2 ± 2.0	A
51	Q2	58.669	35.278	300 ± 50	36.5 ± 6.3	8.2 ± 2.0	A
54*	Q2	58.855	35.263	100 ± 20	36.5 ± 6.3	2.7 ± 0.7	D
58	Q2	58.932	35.251	210 ± 20	36.5 ± 6.3	5.8 ± 1.1	D
61*	Q2	58.965	35.247	190 ± 30	36.5 ± 6.3	5.2 ± 1.2	D
63*	Q2	59.009	35.242	190 ± 30	36.5 ± 6.3	5.2 ± 1.2	D
64	Q2	59.049	35.235	210 ± 50	36.5 ± 6.3	5.8 ± 1.7	C
66*	Q2	59.131	35.22	170 ± 50	36.5 ± 6.3	4.7 ± 1.6	D
67*	Q2	59.323	35.175	70 ± 20	36.5 ± 6.3	1.9 ± 0.6	D
69	Q2	59.497	35.127	0	36.5 ± 6.3	0	-
1	Q1	56.749	35.032	0	12.3 ± 2.9	0	A
3	Q1	57.082	35.129	16 ± 4	12.3 ± 2.9	1.3 ± 0.4	A
4*	Q1	57.317	35.177	15 ± 3	12.3 ± 2.9	1.2 ± 0.4	D
5	Q1	57.44	35.201	12 ± 2	12.3 ± 2.9	1.0 ± 0.3	A
8	Q1	57.473	35.206	25 ± 5	12.3 ± 2.9	2.0 ± 0.6	D
9	Q1	57.481	35.207	15 ± 5	12.3 ± 2.9	1.2 ± 0.5	C
12	Q1	57.5	35.209	29 ± 5	12.3 ± 2.9	2.4 ± 0.7	A
13	Q1	57.507	35.212	20 ± 10	12.3 ± 2.9	1.6 ± 0.9	B
14	Q1	57.519	35.213	27 ± 6	12.3 ± 2.9	2.2 ± 0.7	A
18	Q1	57.558	35.22	18 ± 4	12.3 ± 2.9	1.5 ± 0.5	B
20*	Q1	57.58	35.225	13 ± 3	12.3 ± 2.9	1.1 ± 0.3	D
21*	Q1	57.582	35.225	14 ± 2	12.3 ± 2.9	1.1 ± 0.3	D
23*	Q1	57.615	35.236	25 ± 3	12.3 ± 2.9	2.0 ± 0.5	D
24	Q1	57.864	35.276	50 ± 20	12.3 ± 2.9	4.1 ± 1.9	C
25*	Q1	58.145	35.294	55 ± 5	12.3 ± 2.9	4.5 ± 1.1	D
26	Q1	58.165	35.297	65 ± 15	12.3 ± 2.9	5.3 ± 1.7	A
28	Q1	58.233	35.297	40 ± 10	12.3 ± 2.9	3.3 ± 1.1	A
30*	Q1	58.269	35.297	25 ± 5	12.3 ± 2.9	2.0 ± 0.6	D
32*	Q1	58.282	35.297	30 ± 10	12.3 ± 2.9	2.4 ± 1.0	D
35	Q1	58.304	35.295	50 ± 10	12.3 ± 2.9	4.1 ± 1.3	A
36*	Q1	58.318	35.295	60 ± 20	12.3 ± 2.9	4.9 ± 2.0	D
37	Q1	58.338	35.295	60 ± 10	12.3 ± 2.9	4.9 ± 1.4	A
40*	Q1	58.38	35.289	40 ± 10	12.3 ± 2.9	3.3 ± 1.1	D
41*	Q1	58.395	35.288	10 ± 2	12.3 ± 2.9	0.8 ± 0.3	D
42	Q1	58.4	35.287	0	12.3 ± 2.9	0	A
43	Q1	58.442	35.286	0	12.3 ± 2.9	0	A
44*	Q1	58.443	35.286	13 ± 3	12.3 ± 2.9	1.1 ± 0.3	D
45*	Q1	58.46	35.287	17 ± 2	12.3 ± 2.9	1.4 ± 0.4	D
46	Q1	58.5	35.286	27 ± 10	12.3 ± 2.9	2.2 ± 1.0	B
47	Q1	58.549	35.285	25 ± 5	12.3 ± 2.9	2.0 ± 0.6	A
50	Q1	58.66	35.278	60 ± 10	12.3 ± 2.9	4.9 ± 1.4	A
52	Q1	58.76	35.271	55 ± 5	12.3 ± 2.9	4.5 ± 1.1	A
53	Q1	58.76	35.271	55 ± 5	12.3 ± 2.9	4.5 ± 1.1	B
55	Q1	58.873	35.261	60 ± 10	12.3 ± 2.9	4.9 ± 1.4	B
57	Q1	58.926	35.252	40 ± 10	12.3 ± 2.9	3.3 ± 1.1	D

Table 6. (continued)

Site Number	Surface	Longitude (°E)	Latitude (N°)	Offset (m)	Age (ka)	Slip Rate (mm/yr)	Quality
60*	Q1	58.954	35.248	40 ± 5	12.3 ± 2.9	3.3 ± 0.9	D
62*	Q1	59.009	35.242	50 ± 10	12.3 ± 2.9	4.1 ± 1.3	D
69	Q1	59.497	35.127	0	12.3 ± 2.9	0	-

[a]Slip rates are calculated dividing the geomorphic offset value at each point by the weighted mean CRE age assigned to the corresponding offset surface. Quality letters indicate the reliability of slip rates considering both the offset reconstruction quality and the age relevance. Asterisk marks the sites in which the assignment of offset markers to weighted mean ages determined for the Q1, Q2, and Q3 fan generations is not straightforward.

deeply incising streams form rounded ridges; flat-laying surfaces are too rare and small. This alluvial fan is composed of loosely cemented volcanic clasts. In contrast, the Anabad and Doruneh alluvial fans contain mostly carbonate clasts in different sizes, with some degree of carbonate cementation. This makes the surfaces less erodible such that relatively preserved flat areas are more wide and abundant relative to the Nay surface. Contrary to this fact, a single ^{10}Be age of 102.8 ± 3.8 ka, from the Nay alluvial fan, is older than the five ^{36}Cl exposure ages (~73 to 98 ka) from the Anabad and Doruneh fan surfaces (Figure 7). The slight difference between the maximum ^{36}Cl and ^{10}Be nuclide concentrations could be explained by a higher dissolution rate of the carbonate clasts relative to the quartz-rich volcanic clasts. In summary, the Q3 CRE ages of samples may approach the minimum exposure age of Q3 abandonment surfaces (see section 4.2).

Applying the denudation rate of 7 mm/Ma to two less eroded Anabad and Doruneh Q3 alluvial fan surfaces yields the maximum ^{36}Cl CRE ages ranging from 100 ± 11 to 130 ± 14 ka (Tables 2 and 3). The oldest minimum (103 ± 4.0 ^{10}Be age; no erosion) and maximum (130 ± 14 ka ^{36}Cl age; denudation rate of 7 mm/Ma) CRE ages could represent the lower and upper bounds for the age of the Q3 surface. In this case, the age of 120 ± 20 ka may approach the true age of the Q3 abandonment surfaces.

5. Slip Rates Along the Doruneh Fault System

Cumulative left-lateral displacements recorded by either alluvial fan shape incised by streams or terrace risers were measured at 67 sites (Table 1). The previously discussed in situ-produced ^{10}Be (in quartz-rich clasts) and ^{36}Cl (in carbonate clasts) cosmogenic nuclide concentrations were used to estimate the ages of alluvial abandonment surfaces. The onset of a cumulative offset recorded by main streams incising a surface is assumed to correspond to the age of the host abandonment surface [e.g., *Regard et al*., 2005, 2006; *Authemayou et al*., 2009; *Shabanian et al*., 2009b, 2012b]. For the slip rate calculation from offset terrace risers a debate is ongoing about the age of which terrace could be assigned to the offset riser [e.g., *Tapponnier et al*., 2001; *Cowgill*, 2007; *Kirby et al*., 2007; *Zhang et al*., 2007]. In this paper, slip rates deduced from the offset terrace risers (only in three sites) are based on lower terrace reconstruction [*Cowgill*, 2007] and provide a maximum bound on the slip rate. In total, 67 independent slip rates averaged over ~12 to ~120 ka have been determined along the CFZ and WFZ (Tables 5 and 6 and Figure 11).

At seven sites, Q3 alluvial fans cut by the DFS exhibit the largest cumulative offset (Table 1). From the midlength toward the ends of the CFZ, the measured geomorphic offsets vary from ~850 to ~160 m (Figure 3b). Farther east, at the longitude of 59.497°E, strike-slip faulting dies out. Applying the Q3 surface abandonment age (section 4.2.4) to the offsets recorded by the Q3 surfaces yields left-lateral slip rates of the DFS averaged over the last ~120 ka (Figure 11a), with a maximum rate of 7.1 ± 1.3 mm/yr in the middle of the CFZ decreasing toward the fault zone ends (Figure 11a and Table 5).

At 24 sites along both the CFZ and WFZ, the left-lateral offsets recorded by the Q2 alluvial fans, usually inset in older Q3 alluvial fans, were measured (Figure 3b and Table 1). Along the CFZ, the cumulative displacements observed in the central part and the ends of the fault zone ranged between 300 ± 50 m and 70 ± 20 m, respectively (Figure 3b). Along the WFZ, the Q2 offsets display a slight change from 70 ± 10 m, at the junction with the CFZ, to 25 ± 5 m, near the western end of the fault zone (Figure 3b and Table 1). Applying the 36.5 ± 6.3 ka abandonment age of the Q2 surfaces to these cumulative offsets yields slip rates that vary between 8.2 ± 2.0 and 1.9 ± 0.6 mm/yr (Figure 11b and Table 6); the maximum slip rate is estimated at the midlength of the CFZ (Figure 11b). At the junction between the CFZ and WFZ, the minimum

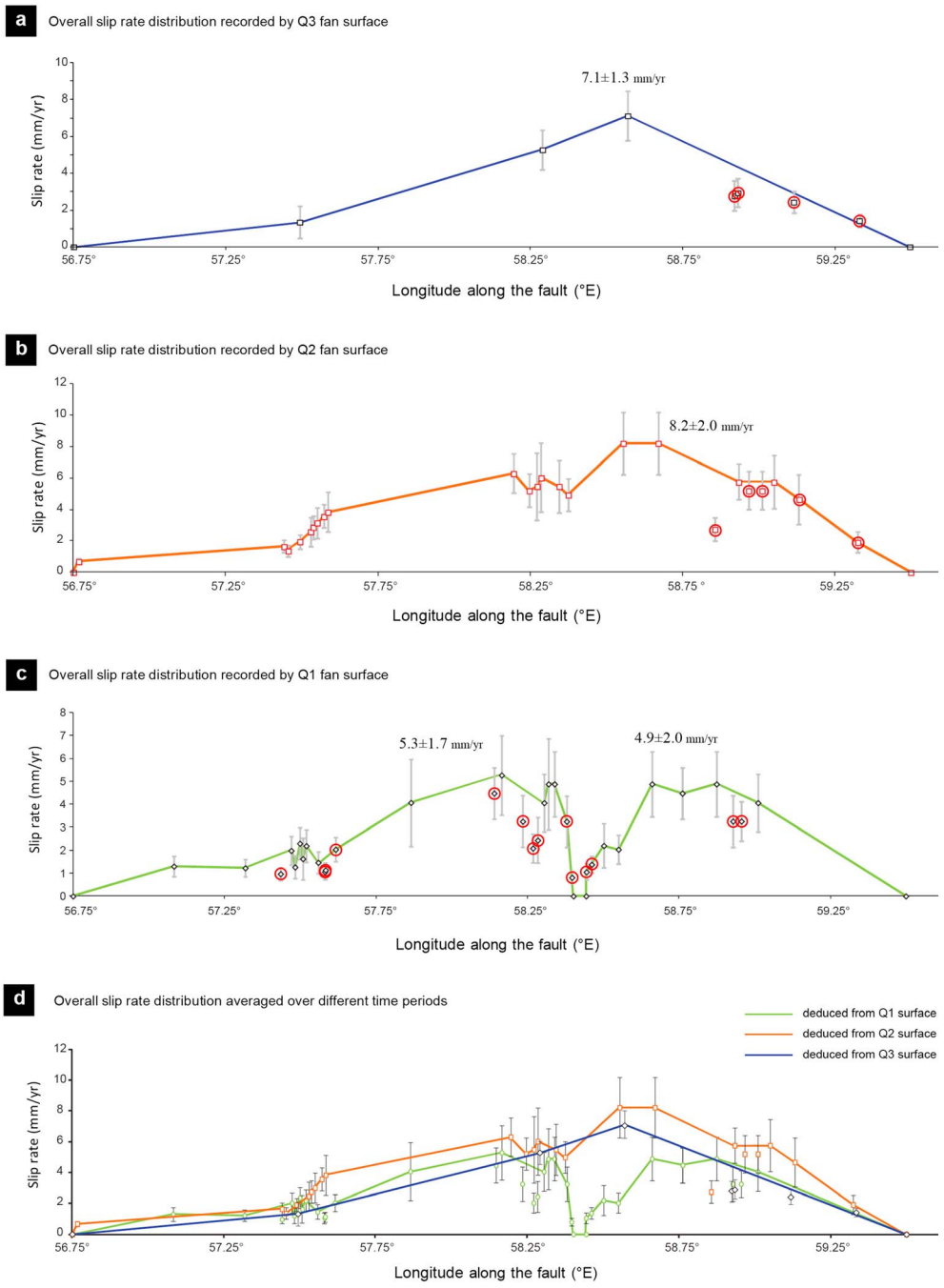

Figure 11. (a–c) Overall slip rate distribution along the central and western part of the DFS, deduced from the age of, and the offsets recorded by the Q3, Q2, and Q1 fan surfaces. Red circles mark the sites in which the assignment of offset markers to weighted mean ages determined for the Q1, Q2, and Q3 fan generations is not straightforward. (d) Along-strike variations in the slip rates averaged over three time periods of ~12, ~36, and ~120 ka.

slip rate of 1.9 ± 0.4 mm/yr along the CFZ corresponds to the maximum slip rate along the WFZ (Figure 11b). This maximum slip rate decreases to 0.7 ± 0.2 mm/yr close to the western termination of the WFZ (Figure 11b). Interestingly, in one site along CFZ (Mazdeh, Figure 6b) the direct slip rate is calculated from dating of an offset alluvial fan surface. It yields a slip rate of 5.5 ± 0.7 mm/yr which is in agreement with the slip rate of 5.2 ± 1.1 mm/yr deduced from the mean abandonment age of Q2 surface at ~36 ka (Table 6 and section 4.3).

Thirty-six left-lateral offsets associated to Q1 alluvial fans, ranging from 10 ± 2 to 65 ± 15 m, have been measured along the DFS (Figure 3b and Table 1). Applying the Q1 surface abandonment age at 12.3 ± 2.9 ka (Figure 11c and Table 6), slip rates ranging from 1.0 ± 0.3 to 5.3 ± 1.7 mm/yr are obtained. The overall trend of the variations in the slip rates averaged over ~12 ka is similar to that of the slip rates averaged over the longer periods of ~36 and ~120 ka. Considering the distribution of slip recorded by the Q1 surfaces, two distinct fault segments are recognized (Figure 11c). Those are separated by a ~4 km long gap along which there is no evidence of faulting on the Q1 surfaces (Figure 4). The slip distribution on a fault segment is mirrored in the other segment showing the same minimum (~1 mm/yr) and maximum (~5 mm/yr) slip rates (Figure 11c). The remnants of Q2 surface on north side of the fault indicate activity of the fault before covering of the fault trace by Q1 and recent alluvial fans (Figure 4).

The three independent sets of slip rate, averaged over ~12, ~36, and ~120 ka (abandonment surface ages of Q1, Q2, and Q3, respectively), show nearly similar overall distributions of slip along both the WFZ and CFZ (Figure 11d). Considering the uncertainties associated to the slip rate estimates, left-lateral slip rates along the WFZ and CFZ may have remained constant at least since the Late Pleistocene. However, at a shorter time scale (during Holocene) the CFZ is divided into the 80 km long west and 100 km long east segments. The boundary between these segments has remained persistent during the Holocene (Figure 11c). Beyond the main fault zone, in rocks armored by Quaternary alluviums, the lack of evidence of active faulting rules out the possibility of slip transfer into fault strands north of the gap. The absence of older Q2 and Q3 surfaces has led to irregular spatial sampling of the slip rate along this part of the fault. This precludes us evaluating the persistency of the gap in deformation before Holocene.

6. Discussion

6.1. Long-Term Geological Versus Short-Term Geodetic Slip Rates

Along the DFS, *Fattahi et al*. [2007] estimated a Holocene slip rate of ~2.5 mm/yr. This estimate is based on an apparent offset of parallel terrace risers at the left bank of the Shesh Taraz River, which are disordered due to left-lateral displacement of the fault (section 4.2). In addition to the complications at their site, as we have shown, a single slip rate would poorly represent the complete DFS slip behavior. *Farbod et al*. [2011] have estimated a short-term left-lateral slip rate of ~2.5 mm/yr using the present-day GPS-derived velocities of KASH and SHIR stations in northeast Iran [*Vernant et al*., 2004; *Masson et al*., 2005, 2007]. This estimate was based on an unproved assumption that the deformation accommodated between the KASH and SHIR stations, north of the DFS, is not significant. The recent GPS measurements in NE Iran [*Mousavi et al*., 2013] reveal interesting facts about current slip rate of the DFS; no significant slip is directly deduced from geodetic measurements [*Mousavi et al*., 2013, Tables 2a and 2b and Figure 2]. However, for the DFS, a maximum current slip rate of 3 mm/yr was deduced from rigid block modeling in which both the northern and southern rigid-assumed blocks are extremely wide and include several active faults in different deformation domains. Moreover, this maximum rate decreases eastward to about 2 mm/yr at the eastern termination of the DFS, where no evidence of left-lateral faulting is observed along the fault [*Farbod et al*., 2011; *Farbod*, 2012; this study]. In summary, there is no consistency between instantaneous geodetic and moderate- to long-term geologic slip rates of the DFS. This discrepancy could be explained in terms of fault slip behavior, temporal scale of measurements, the arrangement and distribution of geodetic arrays relative to geological structures, boundary conditions for rigid block models, etc. Such discrepancies cannot be used for the discrimination of methods which are different in concept and application (e.g., see the gradual improvement of GPS-derived velocity vectors from *Vernant et al*. [2004] to *Mousavi et al*. [2013]). In fact, for phenomena such as after slip that occurs at time scales of months to decades, geodetic studies of similar or longer duration can potentially provide durable insights on short-term crustal deformation. But for problems spanning geological time scales that extend well beyond those of geodetic observation, geodesy can never provide a complete answer [*Burbank and Anderson*, 2012].

An important consequence of our results is that the long-term geological slip rate of the DFS differs from the current slip rate deduced from GPS measurements. The cause of this difference remains unclear. Interestingly, other geological and geodetic studies carried out on several active faults in Iran result in consistent slip rates indicating stable fault activities since Pleistocene (i.e., NE Iran: *Shabanian et al*. [2009a, 2009b, 2012a, 2012b] and *Moussavi et al*. [2013]; Minab-Zendan transfer fault system (SE Iran): *Peyret et al*.

[2009] and *Regard et al*. [2010]; North Tabriz fault system: *Rizza et al*. [2013]; Astaneh-Shahrud fault system: *Djamour et al*. [2010], *Mousavi et al*. [2015], *Javid Fakhr et al*. [2011], and *Hollingsworth et al*. [2010]; and South Main Recent Fault and Kazerun Fault: *Tavakoli et al*. [2008] and *Authemayou et al*. [2009]).

6.2. Seismotectonic Implications

The presented results improve the segmentation model of the DFS proposed by *Farbod et al*. [2011] thanks to the accurate location of (1) the boundaries between the WFZ, CFZ, and EFZ fault zones and (2) the persistent boundary between eastern and western segments of the CFZ. The slip rate varies spatially along the strike of the fault zones (Figure 11d), but the overall distribution of slip rate over the three investigated time periods of ~12, ~36, and ~120 ka is similar, i.e., constant slip rate at a point. This constant pattern implies a homogenous long-term behavior for the western and central zones of the DFS.

The eastern and western fault segments of the CFZ are separated by a persistent boundary (section 5). The 100 km long eastern fault segment slips at 5.3 ± 3 mm/yr and could produce a maximum earthquake of $M_w \approx 7.4$ (deduced from scaling law of *Wells and Coppersmith* [1994]). Along this fault segment, *Farbod et al*. [2011] have presented a coseismic offset of ~4 m recorded by a Qanat line (ancient underground irrigation system). The offset location (longitude of 58.77°E) corresponds to the peak of Holocene cumulative slip of the fault (Figure 11c) and likely represents a maximum coseismic displacement. Such an offset could also be produced by an event as large as $M_w \approx 7.4$, in favor of the characteristic slip behavior. The ~80 km long western segment of the CFZ slips at ~5.3 mm/yr and is capable of producing large earthquakes of $M_w \approx 7.3$. Similarly, the ~70 km long WFZ may produce earthquakes with a maximum magnitude of $M_w \approx 7.2$.

7. Conclusion

The slip distribution along the DFS was established through the systematic measurement of 67 left-lateral offsets recorded by late Quaternary alluvial fan morphologies (i.e., fan surfaces and associated geomorphic features). At six sites, the abandonment ages of three generations of inset Q1, Q2, and Q3 alluvial surfaces were determined using in situ-produced ^{36}Cl and ^{10}Be cosmogenic nuclides at 12.3 ± 2.9 ka, 36.5 ± 6.3 ka, and 120 ± 20 ka, respectively. While local denudation rate was demonstrated negligible, significant inherited cosmogenic nuclide concentrations due to clasts reworked from the upper alluvial fans were evident in the inset Q1 and Q2 surfaces. The relevant ages and geomorphic offsets allowed estimating 67 independent left-lateral slip rates and thus establishing the slip distribution along the CFZ and WFZ during the Late Pleistocene and Holocene.

Along the CFZ, a Late Pleistocene maximum slip rate of 8.2 ± 2.0 mm/yr is estimated, while during Holocene, the fault zone is divided into two fault segments having symmetrical slip rate distribution with respect to their boundary and slipping at 5.3 ± 1.7 mm/yr. The boundary between the eastern and western sectors of the CFZ has remained persistent during the last ~12 ka. The left-lateral slip rate on the reverse-sinistral WFZ is estimated at 1.9 ± 0.4 mm/yr. The seismic segment lengths of the 400 km long DFS vary between ~70 and ~100 km and are thus able to produce earthquakes with magnitudes of $M_w \approx 7.2$–7.4.

Acknowledgments

This work was funded by the INSU-CNRS (France) and the International Institute of Earthquake Engineering and Seismology (IIEES, Iran). Funding was provided by the Dyeti and PNRN programs (INSU-CNRS), as well as ACI FNS program (French Ministry of Research). SPOT images were provided thanks to the ISIS program (©CNES 2007 to 2008, distribution SPOT images S.A.). We thank V. Grimault, D. Lambert, P.A. Lhôte, and the staff of the SCAC of the French Embassy in Tehran for their support. The measurement of ^{10}Be and ^{36}Cl cosmogenic nuclide concentrations, performed at the ASTER AMS national facility (CEREGE, Aix-en-Provence), are supported by the INSU/CNRS, the French Ministry of Research and Higher Education, IRD, and CEA. The ASTER team is acknowledged for the measurements (M. Arnold, K. Keddadouche, and G. Aumaître) and their help (L. Léanni, V. Guillou, and F. Chauvet) to Y.F. during chemical analyses. We are grateful to Jean-François Ritz, three anonymous reviewers, and an Associate Editor for helpful and constructive reviews. The Editor Claudio Faccenna is greatly acknowledged for help and handling the manuscript. All the data presented in this paper are available upon request from the first (Y.F.) or corresponding (E.S.) authors.

References

Alavi-Naini, M., M. J. Vaezi-Pour, N. Alavi Tehrani, A. Behrouzi, and M. H. Kholghi (1992), Geological map of Torbat-e Heidariyeh, 1:250 000, Geol. Surv. of Iran.

Ambraseys, N., and C. Melville (1982), *A History of Persian Earthquakes*, Cambridge Univ. Press, Cambridge, U. K.

Arnold, M., et al. (2010), The French accelerator mass spectrometry facility ASTER: Improved performance and developments, *Nucl. Instrum. Methods Phys. Res., B268*, 1954–1959.

Authemayou, C., et al. (2006), Late Cenozoic partitioning of oblique plate convergence in the Zagros fold-and-thrust belt (Iran), *Tectonics*, *25*, TC3002, doi:10.1029/2005TC001860.

Authemayou, C., et al. (2009), Quaternary slip-rates of the Kazerun and the main recent faults: Active strike-slip partitioning in the Zagros fold-and-thrust belt, *Geophys. J. Int.*, *178*(1), 524–540, doi:10.1111/j.1365-246X.2009.04191.x.

Berberian, M., and R. Yeats (1999), Patterns of historical earthquake rupture in the Iranian Plateau, *Bull. Seismol. Soc. Am.*, *89*(1), 120–139.

Bierman, P. R. (1994), Using in situ produced cosmogenic isotopes to estimate rates of landscape evolution: A review from the geomorphic perspective, *J. Geophys. Res.*, *99*(B7), 13,885–13,896, doi:10.1029/94JB00459.

Brown, E. T., et al. (1991), Examination of surface exposure ages of Antarctic moraines using in situ produced ^{10}Be and ^{26}Al, *Geochim. Cosmochim. Acta*, *55*, 2269–2283.

Brown, E. T., P. Molnar, and D. Broules (2005), Slip-rate measurements on the karakorum fault may imply secular variations in fault motion, *Science*, *309*(5739), doi:10.1126/science.1112508.

Burbank, D. W., and S. Anderson (2012), *Tectonic Geomorphology*, 2nd ed., 454 pp., Blackwell Publ. Ltd.

Calzolari, G. (2015), Spatio-temporal evolution of intraplate strike-slip faulting: The Kuh-e-Faghan Fault, Central Iran, PhD thesis, Roma III Univ.

Calzolari, G., et al. (2015), Spatio-temporal evolution of intraplate strike-slip faulting: The Neogene-Quaternary Kuh-e-Faghan fault, central Iran, accepted in, *Geol. Soc. Am. Bull.*, doi:10.1130/B31266.1.

Chmeleff, J., F. Blanckenburg, K. Kossert, and D. Jakob (2010), Determination of the ^{10}Be half-life by multicollector ICP-MS and liquid scintillation counting, *Nucl. Inst. Methods Phys. Res. B*, *268*(2), 192–199.

Cooke, R. U., A. Warren, and A. Goudie (1993), *Desert Geomorphology*, UCL Press, London.

Cowgill, E. (2007), Impact of riser reconstructions on estimation of secular variation in rates of strike–slip faulting: Revisiting the Cherchen River site along the Altyn Tagh Fault, NW China, *Earth Planet. Sci. Lett.*, *254*, 239–255.

Deino, A., and R. Potts (1992), Age-probability spectra from examination of single-crystal ^{40}Ar/^{39}Ar dating results: Examples from Olorgesailie, Southern Kenya Rift, *Quat. Int.*, *13*(14), 47–53.

Djamali, M., et al. (2011), Application of the Global Bioclimatic Classification to Iran: Implications for understanding the modern vegetation and biogeography, *Ecol. Mediterr.*, *37*(1), 91–114.

Djamour, Y., et al. (2010), GPS and gravity constraints on continental deformation in the Alborz mountain range, Iran, *Geophys. J. Int.*, *183*(3), 1287–1301, doi:10.1111/j.1365-246X.2010.04811.x.

Dunaï, T. J. (2010), *Cosmogenic Nuclides: Principles, Concepts and Applications in the Earth Surface Sciences*, Cambridge Univ. Press, New York.

Dunne, J., D. Elmore, and P. Muzikar (1999), Scaling factors for the rates of production of cosmogenic nuclides for geometric shielding and attenuation at depth on sloped surfaces, *Geomorphology*, *27*(1–2), 3–11.

Eftekhar-Nezhad, J., A. Aghanabati, B. Hamzehpour, and V. Baroyant (1976), Geological map of Kashmar Quadrangle, 1: 250 000, Geol. Surv. of Iran.

Farbod, Y. (2012), Active tectonics of the Doruneh Fault: Seismogenic behavior and geodynamic role, PhD thesis, Aix-Marseille Univ.

Farbod, Y., O. Bellier, E. Shabanian, and M. R. Abbassi (2011), Geomorphic and structural variations along the Doruneh Fault System (Central Iran), *Tectonics*, *30*, TC6014, doi:10.1029/2011TC002889.

Fattahi, M., R. Walker, M. M. Khatib, A. Dolati, and J. Bahroudi (2007), Slip-rate estimates and past earthquakes on the Doruneh fault, eastern Iran, *Geophys. J. Int.*, *168*, 691–709.

Gosse, J. C., and F. M. Phillips (2001), Terrestrial in situ cosmogenic nuclides: Theory and application, *Quat. Sci. Rev.*, *20*, 1475–1560.

Hessami, K., F. Jamali, and H. Tabassi (2003), *Major Active Faults of Iran, 1:2,500,000*, Int. Inst. Earthq. Eng. Seismol., Iran.

Hessami, K., F. Nilforoushan, and C. Talbot (2006), Active deformation within the Zagros Mountains deduced from GPS measurements, *J. Geol. Soc. London*, *163*, 143–148.

Hollingsworth, J., et al. (2010), Active tectonics of the east Alborz mountains, NE Iran: Rupter of the left-lateral Astaneh fault system during the great 856 A.D. Qumis earthquake, *J. Geophys. Res.*, *115*, B12313, doi:10.1029/2009JB007185.

Jackson, J., and D. McKenzie (1984), Active tectonics of the Alpine-Himalayan Belt between western Turkey and Pakistan, *Geophys. J. R. Astron. Soc.*, *77*(1), 185–264.

Javid Fakhr, B., et al. (2011), Fault kinematics and active tectonics at the southeastern boundary of the eastern Alborz (Abr and Khij fault zones): Geodynamic implications for NNE Iran, *J. Geodyn.*, *52*, 290–303.

Kirby, E., et al. (2007), Slip rate gradients along the eastern Kunlun fault, *Tectonics*, *26*, TC2010, doi:10.1029/2006TC002033.

Korschinek, G., et al. (2010), A new value for the half-life of ^{10}Be by heavy-ion elastic recoil detection and liquid scintillation counting, *Nucl. Inst. Methods Phys. Res. B*, *268*(2), 187–191.

Le Béon, M., et al. (2010), Early Holocene and Late Pleistocene slip rates of the southern Dead Sea Fault determined from ^{10}Be cosmogenic dating of offset alluvial deposits, *J. Geophys. Res.*, *115*, B11414, doi:10.1029/2009JB007198.

Le Dortz, K., et al. (2009), Holocene right-slip rate determined by cosmogenic and OSL dating on the Anar fault, Central Iran, *Geophys. J. Int.*, *181*(1), 221–228, doi:10.1111/j.1365-246X.2009.04309.x.

Le Dortz, K., et al. (2011), Dating inset terraces and offset fans along the Dehshir Fault (Iran) combining cosmogenic and OSL methods, *Geophys. J. Int.*, *185*(3), 1145–1174, doi:10.1111/j.1365-246X.2011.05010.x.

Masson, F., et al. (2005), Seismic versus aseismic deformation in Iran inferred from earthquakes and geodetic data, *Geophys. J. Int.*, *160*(1), 217–226, doi:10.1111/j.1365-246X.2004.02465.x.

Masson, F., et al. (2007), Large-scale velocity field and strain tensor in Iran inferred from GPS measurements: New insight for the present-day deformation pattern within NE Iran, *Geophys. J. Int.*, *170*(1), 436–440, doi:10.1111/j.1365-246X.2007.03477.x.

Merchel, S., and U. Herpers (1999), An update on radiochemical separation techniques for the determination of long-lived radionuclide via accelerator mass spectrometry, *Radiochim. Acta*, *84*, 215–219.

Mousavi, Z., et al. (2013), Global Positioning System constraints on the active tectonics of NE Iran and the South Caspian region, *Earth Planet. Sci. Lett.*, *377–378*, 287–298, doi:10.1016/j.epsl.2013.07.007.

Mousavi, Z., et al. (2015), Interseismic deformation of the Shahroud fault system (NE Iran) from space-borne radar interferometry measurements, *Geophys. Res. Lett.*, *42*, 5453–5761, doi:10.1002/2015GL064440.

Nishiizumi, K., et al. (2007), Absolute calibration of ^{10}Be AMS standards, *Nucl. Inst. Methods Phys. B*, *258*, 403–413.

Peyret, M., et al. (2009), Present-day strain distribution across the Minab-Zendan-Palami fault system from dense GPS transects, *Geophys. J. Int.*, *179*, 751–762, doi:10.1111/j.1365-246X.2009.04321.x.

Philip, H., A. Avagyan, A. Karakhanian, J. F. Ritz, and S. Rebai (2001), Estimating slip rates and recurrence intervals for strong earthquakes along an intracontinental fault: Example of the Pambak-Sevan-Sunik fault (Armenia), *Tectonophysics*, *343*, 205–232.

Phillips, F. M., et al. (1997), Cosmogenic ^{36}Cl and ^{10}Be ages of Quaternary glacial and fluvial deposits of the Wind River Range, Wyoming, *Geol. Soc. Am. Bull.*, *109*(11), 1453–1463.

Regard, V., et al. (2005), Cumulative right-lateral fault slip rate across the Zagros–Makran transfer zone: Role of the Minab–Zendan fault system in accommodating Arabia–Eurasia convergence in southeast Iran, *Geophys. J. Int.*, *162*(1), 177–203, doi:10.1111/j.1365-246X.2005.02558.x.

Regard, V., et al. (2006), ^{10}Be dating of alluvial deposits from Southeastern Iran (the Hormoz Strait area), *Palaeogeogr. Palaeoclimatol. Palaeoecol.*, *242*, 36–53, doi:10.1016/j.palaeo.2006.05.012.

Regard, V., et al. (2010), The transition between the Makran subduction and the Zagros collision ranges: Structure and Active deformation, in *Tectonic and Stratigraphic Evolution of Zagros and Makran During the Meso-Cenozoic*, edited by P. Leturmy and C. Robin, *Geol. Soc. London Spec. Publ.*, *330*, 43–64.

Reilinger, R., et al. (2006), GPS constraints on continental deformation in the Africa-Arabia-Eurasia continental collision zone and implications for the dynamics of plate interactions, *J. Geophys. Res.*, *111*, B05411, doi:10.1029/2005JB004051.

Ritz, J. F., E. T. Brown, D. L. Bourlès, H. Philip, A. Schlupp, G. M. Raisbeck, F. Yiou, and B. Enkhtuvshin (1995), Slip rates along active faults estimated with cosmic-ray–exposure dates: Application to the Bogd fault, Gobi-Altaï, Mongolia, *Geology*, *23*(11), 1019–1022.

Ritz, J. F., et al. (2003), Late Pleistocene to Holocene slip rates for the Gurvan Bulag thrust fault (Gobi-Altay, Mongolia) estimated with ^{10}Be dates, *J. Geophys. Res.*, *108*(B3), 2162, doi:10.1029/2001JB000553.

Ritz, J. F., H. Nazari, A. Ghassemi, R. Salamati, A. Shafei, S. Solaymani, and P. Vernant (2006a), Active transtension inside central Alborz: A new insight into northern Iran–southern Caspian geodynamics, *Geology*, *34*(6), 477–480, doi:10.1130/G22319.1.

Ritz, J. F., R. Vassallo, R. Braucher, E. T. Brown, S. Carretier, and D. L. Bourlès (2006b), Using in situ–produced ^{10}Be to quantify active tectonics in the Gurvan Bogd mountain range (Gobi-Altay, Mongolia), *Geol. Soc. Am. Spec. Pap.*, *415*, 87–110, doi:10.1130/2006.2415(06).

Rizza, M., S. Mahan, J. F. Ritz, H. Nazari, J. Hollingsworth, and R. Salamati (2011), Using luminescence dating from coarse matrix material to estimate fault slip-rate in arid domain: Example of the Astaneh Fault (Iran), *Quat. Geochronol.*, *6*(3–4), 390–406.

Rizza, M., et al. (2013), Morphotectonic and geodetic evidence for a constant slip-rate over the last 45 kyr along the Tabriz fault (Iran), *Geophys. J. Int.*, *193*, 1083–1094, doi:10.1093/gji/ggt041.

Schimmelpfennig, I., L. Benedetti, R. Finkel, R. Pik, P.-H. Blard, D. Bourlès, P. Burnard, and A. Williams (2009), Sources of in-situ ^{36}Cl in basaltic rocks, Implications for calibration of production rates, *Quat. Geochronol.*, *4*(6), 441–461.

Schmidt, S., R. Hetzel, J. Kuhlmann, F. Mingorance, and V. A. Ramos (2011), A note of caution on the use of boulders for exposure dating of depositional surfaces, *Earth Planet. Sci. Lett.*, *302*, 60–70.

Shabanian, E., O. Bellier, L. Siame, N. Arnaud, M. R. Abbassi, and J.-J. Cochemé (2009a), New tectonic configuration in NE Iran: Active strike-slip faulting between the Kopeh Dagh and Binalud mountains, *Tectonics*, *28*, TC5002, doi:10.1029/2008TC002444.

Shabanian, E., L. Siame, O. Bellier, L. Benedetti, and M. R. Abbassi (2009b), Quaternary slip rates along the northeastern boundary of the Arabia–Eurasia collision zone (Kopeh Dagh Mountains, Northeast Iran), *Geophys. J. Int.*, *178*(2), 1055–1077, doi:10.1111/j.1365-246X.2009.04183.x.

Shabanian, E., O. Bellier, M. R. Abbassi, L. Siame, and Y. Farbod (2010), Plio-Quaternary stress states in NE Iran: Kopeh Dagh and Allah Dagh-Binalud mountain ranges, *Tectonophysics*, *480*, 280–304, doi:10.1016/j.tecto.2009.10.022.

Shabanian, E., V. Acocella, A. Gioncada, H. Ghasemi, and O. Bellier (2012a), Structural control on volcanism in intraplate post collisional settings: Late Cenozoic to Quaternary examples of Iran and Eastern Turkey, *Tectonics*, *31*, TC3013, doi:10.1029/2011TC003042.

Shabanian, E., et al. (2012b), The Binalud Mountains: A key piece for the geodynamic puzzle of NE Iran, *Tectonics*, *31*, TC6003, doi:10.1029/2012TC003183.

Siame, L., et al. (1997), Cosmogenic dating ranging from 20 to 700 ka of a series of alluvial fan surfaces affected by the El Tigre fault, Argentina, *Geology*, *25*(11), 975–978.

Solaymani Azad, S., J. F. Ritz, and M. R. Abbassi (2011), Left-lateral active deformation along the Mosha-North Tehran fault system (Iran): Morphotectonics and Paleoseismological investigations, *Tectonophysics*, *497*, 1–14, doi:10.1016/j.tecto.2010.09.013.

Stone, J. O. (2000), Air pressure and cosmogenic isotope production, *J. Geophys. Res.*, *105*(B10), 23,753–23,759, doi:10.1029/2000JB900181.

Stone, J. O., G. L. Allan, L. K. Fifield, and R. G. Cresswell (1996), Cosmogenic chlorine-36 from calcium spallation, *Geochim. Cosmochim. Acta*, *60*, 679–692.

Talebian, M., and J. Jackson (2002), Offset on the Main Recent Fault of NW Iran and implications for the late Cenozoic tectonics of the Arabia–Eurasia collision zone, *Geophys. J. Int.*, *150*(2), 422–439, doi:10.1046/j.1365-246X.2002.01711.x.

Tapponnier, P., F. J. Ryerson, J. Van der Woerd, A. S. Mériaux, and C. Lasserre (2001), Long-term slip rates and characteristic slip: Keys to active fault behavior and earthquake hazard, *Earth Planet. Sci. Lett.*, *333*, 483–494.

Tavakoli, F., et al. (2008), Distribution of the right-lateral strike-slip motion from the Main Recent Fault to the Kazerun Fault System (Zagros, Iran): Evidence from present-day GPS velocities, *Earth Planet. Sci. Lett.*, *275*(3–4), 342–347.

Taylor, J. R. (1997), *An Introduction to Error Analysis, the Study of Uncertainties in Physical Measurements*, Univ. Sci. Books, Sausalito, Calif.

Tchalenko, J. S., M. Berberian, and H. Behzadi (1973), Geomorphic and seismic evidence for recent activity on the Doruneh Fault, Iran, *Tectonophysics*, *19*, 333–341.

Thomas, D. S. G. (1989), *Arid Zone Geomorphology*, Halsted Press, New York.

Vernant, P., et al. (2004), Present-day crustal deformation and plate kinematics in the Middle East constrained by GPS measurements in Iran and northern Oman, *Geophys. J. Int.*, *157*(1), 381–398, doi:10.1111/j.1365-246X.2004.02222.x.

Walker, R., and J. Jackson (2004), Active tectonics and late Cenozoic strain distribution in central and eastern Iran, *Tectonics*, *23*, TC5010, doi:10.1029/2003TC001529.

Ward, G. K., and S. R. Wilson (1978), Procedures for comparing and combining radiocarbon age determinations: A critique, *Archaeometry*, *20*(1), 19–31.

Wellman, H. W. (1966), Active wrench faults of Iran Afghanistan and Pakistan, *Geologische Undschau*, *55*, 716–735.

Wells, D., and K. J. Coppersmith (1994), New empirical relationships among magnitude, rupture length, rupture width, rupture area, and surface displacement, *Bull. Seismol. Soc. Am.*, *84*(4), 974–1002.

Wells, S. G., L. D. McFadden, J. Poths, and C. T. Olinger (1995), Cosmogenic 3He exposure dating of stone pavements: Implications for landscape evolution in deserts, *Geology*, *23*, 613–616.

Zhang, P. Z., P. Molnar, and X. Xu (2007), Late quaternary and present-day rates of slip along the Altyn Tagh Fault, northern margin of the Tibetan Plateau, *Tectonics*, *26*, TC5010, doi:10.1029/2006TC002014.

Zreda, M. G., F. M. Phillips, and D. Elmore (1994), Cosmogenic ^{36}Cl accumulation in unstable landforms, 2. Simulations and measurements on eroding moraines, *Water Resour. Res.*, *30*, 3127–3136, doi:10.1029/94WR00760.